

R97-5.903.0008-9

*Evaluation of Structural Porous Metals*

**FINAL REPORT**

Prepared for:  
Department of Navy  
Office of Naval Research  
Arlington, VA 22217

Under Contract No. N00014-95-C-0231

Mark S. Thompson  
Mark L. Renauld

December 10, 1997

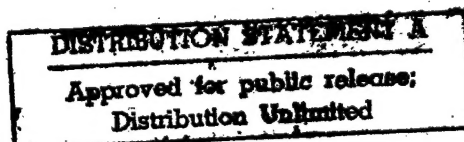
The views and conclusions contained in this document are those of the authors and should not be interpreted as necessarily representing the official policies, either expressed or implied, of the Defense Advanced Research Projects Agency of the U.S. Government.



**United  
Technologies**

Research Center

19980102 010



DTIC QUALITY INSPECTED 4

# REPORT DOCUMENTATION PAGE

Form Approved  
OMB No. 0704-0188

Public reporting burden for this collection of information is estimated to average 1 hour per response, including the time for reviewing instructions, searching existing data sources, gathering and maintaining the data needed, and completing and reviewing the collection of information. Send comments regarding this burden estimate or any other aspect of this collection of information, including suggestions for reducing this burden, to Washington Headquarters Services, Directorate for Information Operations and Reports, 1215 Jefferson Davis Highway, Suite 1204, Arlington, VA 22202-4302, and to the Office of Management and Budget, Paperwork Reduction Project (0704-0188), Washington, DC 20503.

1. AGENCY USE ONLY (Leave blank)		2. REPORT DATE 10-Dec-97		3. REPORT TYPE AND DATES COVERED Final Report 11-Oct-95 - 10-Oct-97	
4. TITLE AND SUBTITLE EVALUATION OF STRUCTURAL POROUS METALS				5. FUNDING NUMBERS N00014-95-C-0231	
6. AUTHOR(S) Mark S. Thompson and Mark L. Renauld					
7. PERFORMING ORGANIZATION NAME(S) AND ADDRESS(ES) United Technologies Corporation United Technologies Research Center 411 Silver Lane East Hartford, CT 06108				8. PERFORMING ORGANIZATION REPORT NUMBER R97-5.903.0008-9	
9. SPONSORING/MONITORING AGENCY NAME(S) AND ADDRESS(ES) Department of the Navy Office of Naval Research Arlington, VA 22217				10. SPONSORING/MONITORING AGENCY REPORT NUMBER	
11. SUPPLEMENTARY NOTES					
12a. DISTRIBUTION / AVAILABILITY STATEMENT The views and conclusions contained in this document are those of the authors and should not be interpreted as necessarily representing the official policies, either expressed or implied, of the Advanced Research Projects Agency of the U.S. Government.				12b. DISTRIBUTION CODE	
13. ABSTRACT (Maximum 200 words)  Porous metals possess a number of attractive property attributes that may enhance current system capabilities. These include mechanical properties, energy absorption properties, acoustic attributes and thermal properties. There is continuing work to evaluate key performance characteristics such as corrosion resistance and fatigue behavior. In this program, two new commercial products are studied, aluminum alloy foam from Austrian Metal Company (AMAG) and aluminum (A356) and nickel (Hastelloy-X) alloy Lattice Block Material (LBM™) from JAMCORP. These materials were evaluated for their macrostructural features, microstructural characteristics and mechanical performance. The aluminum foam, equivalent to 6061 aluminum alloy, was fabricated in both plate and cylindrical forms at two densities ranges. All product forms exhibit variation in macrostructure which causes significant variation in the measured compression, tension and bending properties. In general, the experimental data compare well with the models of Gibson & Ashby. In contrast, the LBM™ product shows an extremely repeatable structure which leads to superior compression and bending properties coupled with reduced data scatter. Using bulk parent metal stress-strain properties, finite element model predictions correlate well with experimental findings. Additional prediction are made for the effect of unit cell size, ligament diameter and parent metal strength on the performance of LBM™.					
14. SUBJECT TERMS porous metal, metal foam, aluminum, lattice block material testing, finite element model				15. NUMBER OF PAGES 50	
				16. PRICE CODE	
17. SECURITY CLASSIFICATION OF REPORT Unclassified	18. SECURITY CLASSIFICATION OF THIS PAGE Unclassified	19. SECURITY CLASSIFICATION OF ABSTRACT Unclassified	20. LIMITATION OF ABSTRACT SAR		



**United  
Technologies**

**Research Center**

**R97-5.903.0008-9**

*Evaluation of Structural Porous Metals*

Reported by: Mark S. Thompson  
Mark S. Thompson

Mark L. Renauld  
Mark L. Renauld

Approved by: Earl R. Thompson  
Earl R. Thompson

**DATE: December 10, 1997**

**Per STEVEN FISHMAN  
ONR/Code 332  
1/7/98**

## TABLE OF CONTENTS

1.0	INTRODUCTION.....	1
2.0	EVALUATION OF AMAG POROUS ALUMINUM .....	2
2.1	Introduction.....	2
2.2	Macroscopic Porous Aluminum Evaluation .....	3
2.3	Microstructural Porous Aluminum Evaluation.....	11
2.4	Mechanical property Evaluation.....	12
2.5	Summary .....	18
3.0	EVALUATION OF LATTICE BLOCK MATERIAL™ .....	19
3.1	Introduction.....	19
3.2	Macrostructural Analysis of LBM™ .....	20
3.3	Microstructural Analysis of LBM™ .....	21
3.4	Structural Evaluation of Lattice Block Material™.....	25
3.5	Finite Element Modeling of Lattice Block Material™.....	29
3.6	Summary .....	34
4.0	CONCLUSIONS .....	35
5.0	ACKNOWLEDGEMENTS .....	36
	APPENDIX A .....	37
	APPENDIX B .....	48
	APPENDIX C .....	49



## CHAPTER 10 INTRODUCTION

Structural porous metals (SPM) have recently gained significant interest due to a potentially attractive combination of weight and structural performance. Further, manufacturing advances currently allow the laboratory production of SPM over a relative density range from several percent to nearly 100 percent from various parent metals including aluminum, iron, nickel and titanium. Additional application flexibility is realized with porous metal fabricated in either an open cell or closed cell configuration whereby the prevention or acceptance of fluid flow through the material, heat insulation or conduction and mechanical performance capability may be desired.

The original tasks of this program were to i) fabricate and evaluate a 2000 series aluminum SPM and perform critical evaluation tests on the product and ii) test a government furnished porous metal product, perhaps a Ti-based SPM manufactured by McDonnell Douglas. Since the start of the ONR contract, there have been several significant developments resulting in a redirection request by UTRC and approval by ONR. First, the Austrian Metals Company (AMAG) and the Fraunhofer Institute (Bremen, Germany) are marketing closed cell, structural porous aluminum manufactured fundamentally identical to the original UTRC process, powder blending, consolidation, foaming and heat treatment. Therefore SPM production was terminated at UTRC and plate and cylinder material was purchased from AMAG for evaluation by UTRC in Task I. A summary of work performed under the original Task I is summarized in Appendix A. Second, McDonnell Douglas encountered difficulty providing material for UTRC to perform Task II. Simultaneously, UTRC learned that Jonathan Aerospace Materials Corporation (JAMCORP) has recently made dramatic progress in the development of lattice block materials (LBM™'s) which is a very repeatable structure consisting of repeating internal nodes and high levels of 'porosity'. At least one processing technique has the flexibility to allow for processing of castable aluminum, iron and nickel alloys. Based on these potentials, UTRC and ONR redirected Task II to the evaluation of aluminum and high temperature LBM™ samples as summarized in Appendix B.

The following report summarizes three general assessments, namely macroscopic, microstructural and mechanical performance, used to evaluate the AMAG SPM and JAMCORP LBM™. A structural performance model developed by Gibson and Ashby is used for mechanical property data comparisons. Since the LBM™ is a regular, repeating structure, finite element analysis models are used to predict the effect of modifications to the LBM™ such as unit cell size, ligament diameter and parent metal properties.

## 20 EVALUATION OF AMAG POROUS ALUMINUM

### 21 Introduction

The AMAG manufacturing process is based on powder blending, extrusion processing and a heat treatment cycle as illustrated in Figure 2.1-1, and is fundamentally identical to the process that UTRC had practiced in the original program, prior to the redirection. The objective of this task was changed to evaluate AMAG plate and cylinder material in terms of macrostructure, microstructure and mechanical properties.

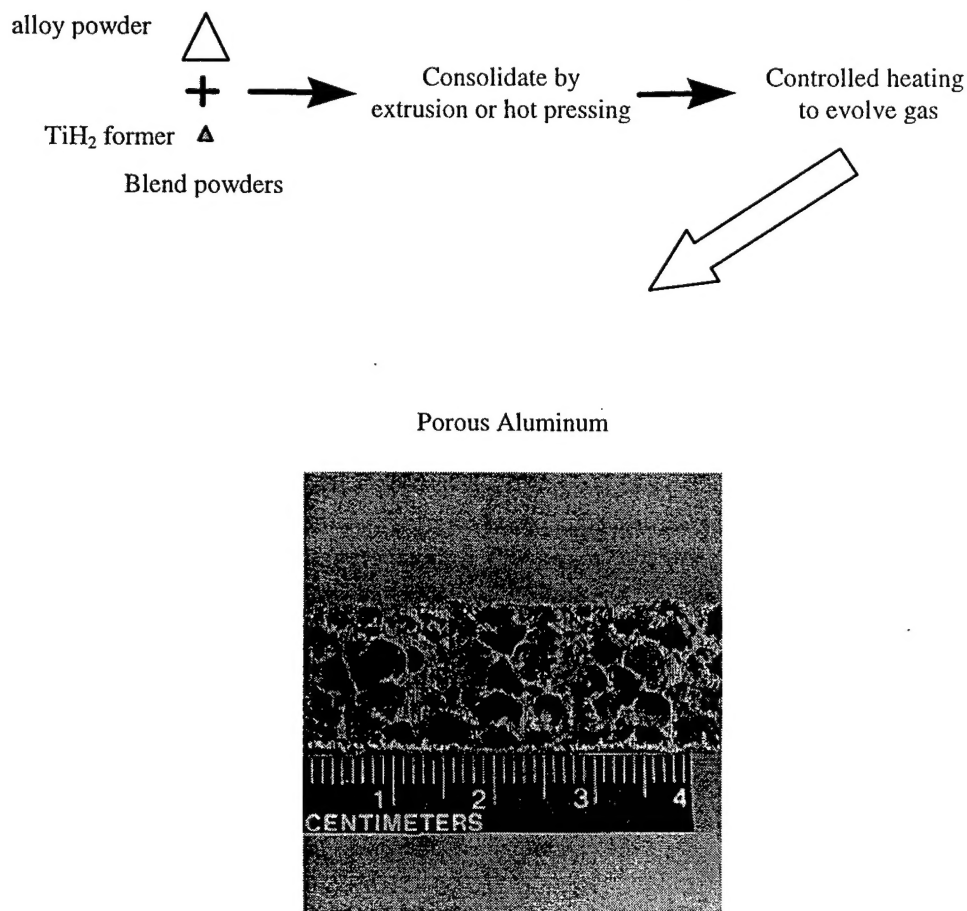


Figure 2.1-1 AMAG manufacturing process schematic.

AMAG porous aluminum was purchased in one chemistry (Aluminum alloy 6061 T5), two density ranges (0.4-0.5g/cc and 0.6-0.75g/cc) and two forms (plate and cylinder) as summarized in the following table. As practiced by AMAG, the density of porous metal is defined by the mass of extruded material placed in a closed tool of known volume. The differences between the specified and received density result from several sources, which appear to be more significant at densities below 0.55 g/cc. These sources include metal drainage from tool, incomplete filling of tool, shrinkage on cooling, tool deformation during expansion and incomplete decomposition of the  $\text{TiH}_2$  foaming agent.

**TABLE 21-1**  
**AMAG MATERIAL SUMMARY**

<i>Product Form</i>	<i>Quantity</i>	<i>Specified Geometry (mm)</i>	<i>Specified Density (g/cc)</i>	<i>Actual Density (g/cc)</i>
<i>Plate</i>	<i>3</i>	<i>500X500X15</i>	<i>0.405</i>	<i>0.51-0.61</i>
<i>Plate</i>	<i>3</i>	<i>500X500X15</i>	<i>0.6-0.75</i>	<i>0.70-0.78</i>
<i>Cylinder</i>	<i>5</i>	<i>50 diameter X 200 height</i>	<i>0.6-0.75</i>	<i>0.39-0.41</i>

## 2.2 Macroscopic Porous Aluminum Evaluation

Macroscopic evaluation began with as-received dimensional and mass documentation on each panel and cylinder for density calculation. Numerous sections throughout the plates and cylinders were also taken to document product inconsistencies and abnormalities. In particular, there exists a significant variation in cell size with location in the product as contrasted by Figure 2.1-1 where pores are nearly the same size and Figure 2.2-1 where significantly different pore sizes exist. In fact, several sections revealed a single pore which extended across the entire thickness of a plate, that is, from one edge skin to the other. Figures 2.3-2 through 2.3-4 show additional defects observed in the plates and cylinders. Cell walls commonly contain breaks, tears, curvatures and wrinkles. Walls between adjacent cells are often not integral, rather material is simply pressed together, containing visible gaps. Within cell walls, porosity is prevalent and widely dispersed. The skin thickness shows significant variation, roughness and occasional breaks.

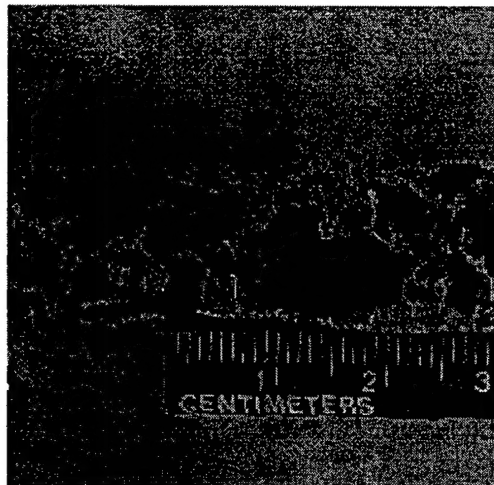


**Figure 2.2-1 Pore size variation in AMAG porous aluminum.**



**Figure 2.2-2 Cross section of AMAG aluminum foam showing non-uniform material distribution, cell distortion, cell wall tearing and cell wall wrinkling**

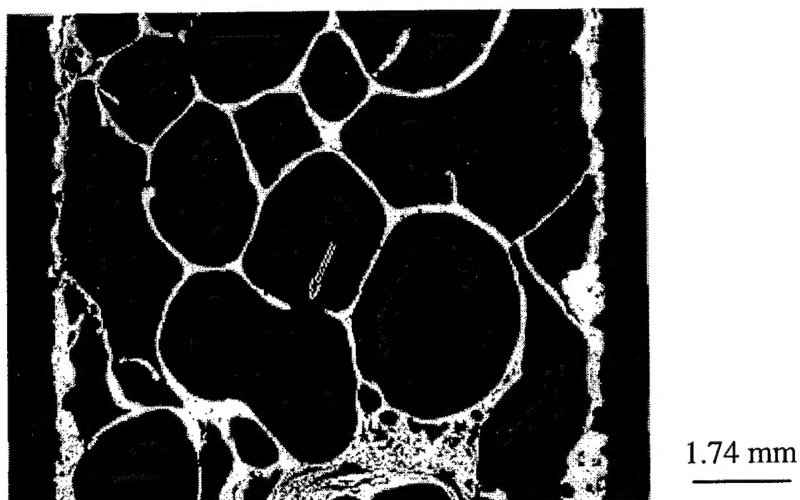


**Figure 2.2-3 AMAG aluminum foam (in epoxy) with broken cell walls, cell wall curvature, broken skin and variation in skin thickness.**

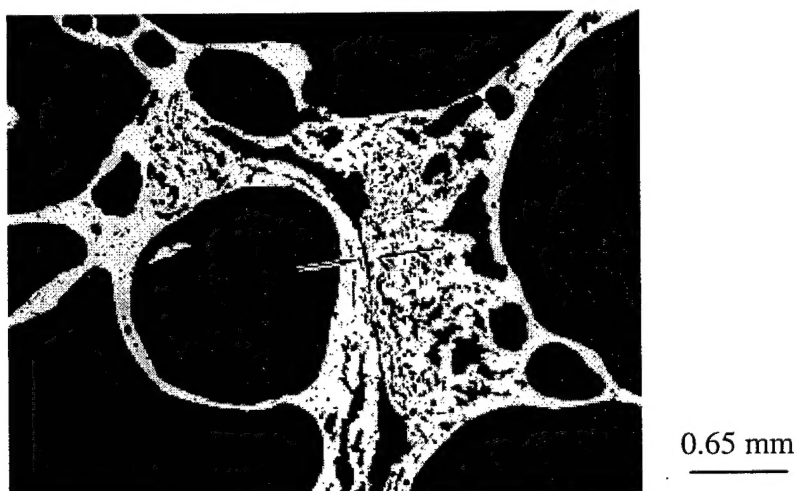


**Figure 2.2-4 AMAG foam sample (in epoxy) with cell wall porosity and lack of junction between cell walls.**

Image analysis techniques were then employed to compare the cell wall thickness and cell size variations in the high and low density plates and the cylinders. For the plate product, five edge sections and five mid-plate sections were taken from a high and a low density panel. Six sections were extracted from a cylinder, 4 from the ends and 2 from the middle. Figure 4.2-5 and 2.2-6 show the plate and cylinder locations of the samples. All sections were slow-cut on a band saw with a fine tooth blade and were then infiltrated with cold-mount epoxy and ground to remove any damage introduced during the cutting process, typically 0.75-1.5mm. Red dye(Rhodamine-B) was mixed with the mounting epoxy to enhance optical contrast between the cell walls and epoxy-filled pores. Tables 2.2-1 through 2.2-4 summarize the number of samples, the total number of measurements, average value and standard deviation of the values taken from

each product form in each location where the abbreviations HDPe, HDPm, LDPe, LDPm, Cb, Cm and Ct refer to the high density plate edge, high density plate middle, low density plate edge, low density plate middle, cylinder bottom, cylinder middle and cylinder top, respectively. It is important to note that the cylinder designations “top” and “bottom” do **not** refer to any extrusion or foaming orientation, rather they are simply labels for identification purposes.

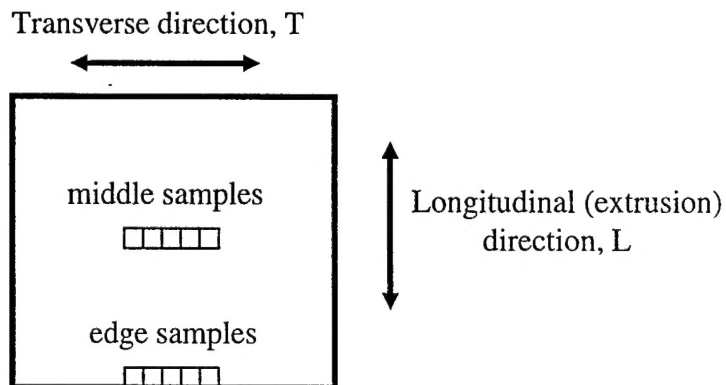


Figure 2.2-5 Plate samples extracted for image analysis.

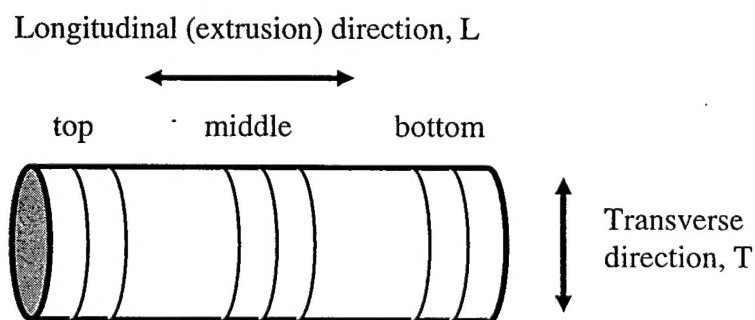


Figure 2.2-6 Cylinder samples extracted for image analysis.

**Table 2.2-1**  
**Summary of "L" Wall Thickness Measurements**

Product and Sample Location	Number of Samples	Number of Measurements	Average (mm)	Standard Deviation (mm)
HDPe	5	558	0.87	0.51
HDPm	5	505	0.89	0.54
LDPe	5	252	0.98	0.54
LDPm	5	379	0.91	0.47
Cb	2	91	2.52	1.42
Cm	2	123	1.48	1.22
Ct	2	142	1.43	0.69

**Table 2.2-2**  
**Summary of "T" Wall Thickness Measurements**

Product and Sample Location	Number of Samples	Number of Measurements	Average (mm)	Standard Deviation (mm)
HDPe	5	413	0.89	0.52
HDPm	5	523	0.95	0.67
LDPe	5	236	0.99	0.52
LDPm	5	403	0.93	0.53
Cb	2	191	1.65	0.78
Cm	2	240	1.57	1.22
Ct	2	265	1.64	0.78

**Table 2.2-3**  
**Summary of "L" Cell Area Measurements**

Product and Sample Location	Number of Samples	Number of Measurements	Average (mm <sup>2</sup> )	Standard Deviation (mm <sup>2</sup> )
HDPe	5	220	3.93	6.41
HDPm	5	442	2.59	3.71
LDPe	5	196	5.49	9.41
LDPm	5	223	4.45	5.48
Cb	2	111	9.27	21.16
Cm	2	101	6.88	13.1
Ct	2	92	4.62	6.09

**Table 2.2-4**  
**Summary of "T" Cell Area Measurements**

Product and Sample Location	Number of Samples	Number of Measurements	Average (mm <sup>2</sup> )	Standard Deviation (mm <sup>2</sup> )
HDPe	5	240	2.70	4.80
HDPm	5	383	2.85	3.87
LDPe	5	248	4.58	6.84
LDPm	5	292	4.13	4.68
Cb	2	291	12.19	24.02
Cm	2	238	8.26	25.38
Ct	2	213	6.92	9.64



The cell size and wall thickness measurements within a sample, location and product all contain significant scatter such that an analysis of variance (ANOVA) routine was used to statistically compare measurements taken under two different categories. In this context, category refers to different locations within a product form (plate or cylinder) or different density plates with measurements taken in the same location, edge or middle. The nested linear model described by equation 2.2.1 is used for the analysis:

$$y_{ijk} = \mu + \alpha_i + \beta_{j(i)} + \varepsilon_{(ij)k} \quad (2.2.1)$$

where:  $y_{ijk}$  =  $k^{\text{th}}$  measured values for  $i^{\text{th}}$  category and  $j^{\text{th}}$  sample

$\mu$  = mean effect

$\alpha_i$  = category effect for high and low density plate comparison or for location comparisons within a plate or cylinder ( $i = 1, \dots, a$ ;  $a = 2$ )

$\beta_{j(i)}$  = effect of the  $j^{\text{th}}$  specimen within a category ( $j=1, \dots, b$ ;  $b=2$  or  $5$ )

$\varepsilon_{ijk}$  = error

**Table 2.2-5 ANOVA**

Source	Sum of Squares (SS)	Degrees of Freedom (df)	Mean Square (MS=SS/df)
Category	$\sum_{i=1}^a \frac{y_{i..}^2}{n_{i..}} - \frac{y_{...}^2}{n_{..}}$	$a - 1$	MS Density
Specimen (within category)	$\sum_{i=1}^a \sum_{j=1}^b \left[ \frac{y_{ij.}^2}{n_{ij.}} \right] - \sum_{i=1}^a \frac{y_{i..}^2}{n_{i..}}$	$a(b - 1)$	MS Specimen
Error	$\sum_{i=1}^a \sum_{j=1}^b \sum_{k=1}^{n_{ij}} y_{ijk}^2 - \sum_{i=1}^a \sum_{j=1}^b \frac{y_{ij.}^2}{n_{ij.}}$	$(n_{..} - 1) - (a - 1) - a(b - 1)$	MS Error
Total	$\sum_{i=1}^a \sum_{j=1}^b \sum_{k=1}^{n_{ij}} y_{ijk}^2 - \frac{y_{...}^2}{n_{..}}$	$n_{..} - 1$	MS Total

Once the mean square density and mean square specimen is computed from any two sets of data, the F statistic is computed according to:

$$F = \text{MS Category} / \text{MS Specimen (within category)} \quad (2.2.2)$$

The intent is to test the null hypothesis:

$H_0$ : There is no difference between the categories.

vs.

$H_1$ : The categories are different.

The 95% and 99% cutoff values for F with  $a=2$  (comparison between two categories) and  $b=5$  (five samples per location in a given plate) are 5.32 and 11.26, respectively. With  $a=2$  (comparison between two categories) and  $b=2$  (two samples per location in a cylinder) the 95% and 99% cutoffs for F are 18.51 and 98.5, respectively. If the computed F value exceeds the cutoff, the null hypothesis is rejected at the corresponding level of significance, that is, that the two categories are indeed independent at the selected level of significance. If the computed F value does not exceed the cutoff, we fail to reject the null hypothesis and conclude that the data do not have evidence that the two categories are different.

The above procedure was applied to both the cell wall thickness measurements and the cell area measurements summarized in Tables 2.2-1 through 2.2-4 for the plate and cylinder product forms sectioned transversely and longitudinally. Again, the designations "top" and "bottom" do **not** refer to any extrusion or foaming orientation, rather they are simply labels for identification purposes.

Large values of the F distribution indicate a high probability that the two populations are not the same. Therefore F values from two populations from within the same type of plate or cylinder are ideally small since this indicates little variability within the product form. Similarly, large F values computed between a low and a high density plate population provides evidence for the density difference. For example, the low density plate may be lower density due to larger cells and/or thinner cell walls. Tables C.1-C.4 summarize the calculated F-statistics.

Overall, the ANOVA results indicate there is little difference in the measured wall thicknesses within a given plate and between high and low density plate at the same location. The main exception is the comparison between the edge and middle measurements made on the high density plate. There is also a reasonable probability, although less than 95%, that the wall thickness measurements from the middle of the high and low density plates are different. Considering the cell area data, a high probability exists that the longitudinal cell size at the edge and in the middle of high and low density plates is different.

The only statistically meaningful comparison on the cylinders are a wall thickness comparison between middle and end sections and a cell area comparison between middle and end sections. Other comparisons suggests sufficient variability within a sample and from sample to sample that location to location conclusions cannot be drawn at a 95% confidence level.

### 2.3 Microstructural Porous Aluminum Evaluation

AMAG fabricates the last treatable aluminum-based foam with a variety of magnesium and silicon additions. An aluminum-magnesium-silicon alloy similar to 6061 was selected as the target material in conjunction with a T5 heat treatment which consists of 14 hours at 160°C.

Wet chemical analysis was performed by Dirats Laboratories (Westfield, MA) on a heat treated plate sample via inductively couple plasma emission, or ICP with the results summarized in Table 2.3-1. The typical microstructure of the foam is shown in Figure 2.3-1 wherein dark particles such as those labeled "A" and "B" are surrounded by a gray outer-layer. These second phase compositions were determined by microprobe analyses as Ti-rich (95.8 wt.%) particles encompassed by an Al-43.6Ti-2Si-0.2Mg phase. The dark Ti-rich particles are probably  $\text{TiH}_2$  particles which have not fully reacted during foaming. Particles up to 20 $\mu\text{m}$  in diameter were observed. This is similar to the  $\text{TiH}_2$  particle size reported by AMAG, 10-15 $\mu\text{m}$  with some large as 40 $\mu\text{m}$ . The microprobe is incapable of detecting hydrogen, thereby explaining the lack of hydrogen reported by this instrument.

The surrounding phase Al-43.6 Ti-2Si-0.2Mg probably formed during foaming or subsequent heat treatment from the interdiffusion between the Al-Si-Mg matrix and the Ti-rich particle. Small dark circular locations of porosity are also dispersed throughout the matrix.

TABLE 23-1  
AMAG POROUS AL CHEMICAL COMPOSITION(WT%)

Element	6061	AMAG Foam	Element	6061	AMAG Foam
<i>Si</i>	0.4-0.8	0.63	<i>Zn</i>	0.25 max	0.03
<i>Fe</i>	0.7 max	0.23	<i>Ti</i>	0.15 max	0.80
<i>Cu</i>	0.15-0.40	0.01	<i>Cr</i>	0.04-0.35	0.01
<i>Mn</i>	0.15 max	<0.01	<i>Ni</i>		0.02
<i>Mg</i>	0.8-1.2	1.53	<i>Al</i>	Bal.	Bal.



**Figure 2.3-1 Typical AMAG porous aluminum microstructure (500X).**

## **2.4 Mechanical Property Evaluation**

In evaluation of the AMAG porous aluminum mechanical performance, plate and cylinder samples were loaded in compression, in tension and in bending (3- and 4-pt) at room temperature in laboratory air. Compression samples were cut from plate material such that the compression axis was through-thickness, transverse and longitudinal to the extrusion direction which, using plate notation is simplified as S, T and L, respectively. Compression samples were also fabricated to compress the cylindrical material axially. Flat tensile samples were machined from the foam plates in the L orientation (Figure 2.4-1) and cylindrical tension specimens were fabricated from the cylinders (Figure 2.4.2). Bend specimens, 3- and 4- pt, were cut in both the L and T orientations. All test samples contained the original foam skin except the cylindrical tensile specimens for which the diameter was reduced and the skin was removed in the process. The skin is expected to provide additional compression strength and stiffness in the T and L orientations, but not in the S direction. Additional bending strength and stiffness, regardless of specimen orientation, may also result from leaving the skin on the foam. The number of cells within a given test specimen was limited by the typical cell size, 3-5mm and the thickness of the plate, 13-15 mm.

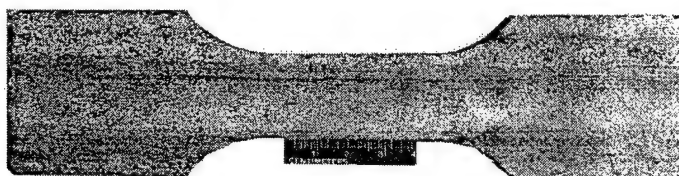


**Figure 2.4-1 Flat tensile specimen cut from AMAG foam plate.**

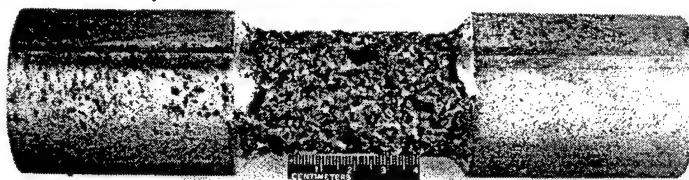


**Figure 2.4-2 Cylindrical tensile specimen machined from AMAG foam cylinder.**

All compression and bending tests were performed at a constant crosshead displacement rate of 1.27 mm/min and 2.54 mm/min, respectively, with force measured by a load cell and deflection monitored by a deflectometer mounted directly under the moving crosshead. Most mechanical test specimens were unloaded to zero force and reloaded throughout the test to monitor modulus changes with deformation. Prior to each compression test, a thin sheet (75 $\mu$ m) of soft, high purity aluminum was placed between the sample and the compression platens to improve contact between the specimens and platens and enhance data quality at low load. All load-deflections curves were recorded using X-Y recorders.

For the bending tests, rectangular plates measuring 9.5mm wide and 3.3mm thick were placed between the test specimen and load pins. Under 3-pt. bend loading, the lower span,  $l_s$ , was typically 10 times the average specimen height ( $l_s=10h$ ). Two tests were performed with  $l_s=25h$ . Under 4-pt bending, the outer and inner spans were maintained at 10h and 5h, respectively.

During this test program, a total of 21 compression tests, 6 tension tests, 19 3-pt bend tests, 4 4-pt bend tests and 10 3-pt bend fatigue tests were performed. Nominal compression and tensile stress and strain values were calculated from standard ASTM formulas derived for solid test pieces:

$$\sigma_f = \frac{F}{A} \quad (2.4.1)$$

and

$$\epsilon = \frac{\Delta h}{h_o} \quad (2.4.2)$$

where  $F$  is the total force applied to the specimen,  $A$  is the overall specimen cross-section,  $\sigma_f$  is the apparent sample stress,  $\Delta h$  is the change in sample height and  $h_o$  is the initial sample height. The foam modulus,  $E_f$ ,

$$E_f = \frac{\sigma_f}{\epsilon} \quad (2.4.3)$$

was calculated from the initial  $\sigma$ - $\epsilon$  loading path and after 10% or 1% compression or tensile strain, respectively. In compression, the foam plateau stress,  $\sigma_p$ , was measured as the intersection

of the initial modulus line and a line parallel to the plateau in the  $\sigma$ - $\epsilon$  curve. Figure 2.4-3 illustrates the extraction of compression data from a compressive stress-strain curve. Under bending and tension loading, the maximum stress was taken as the foam stress.

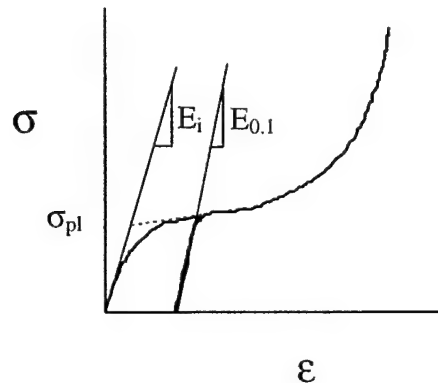
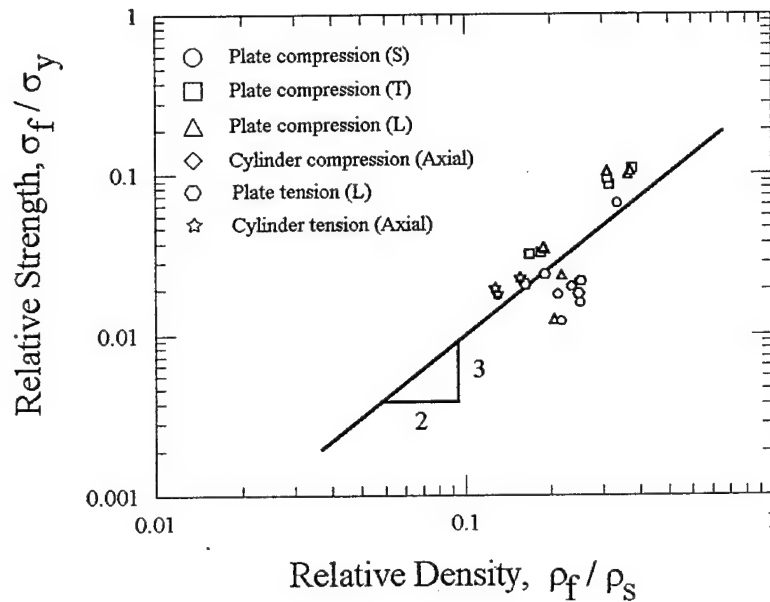


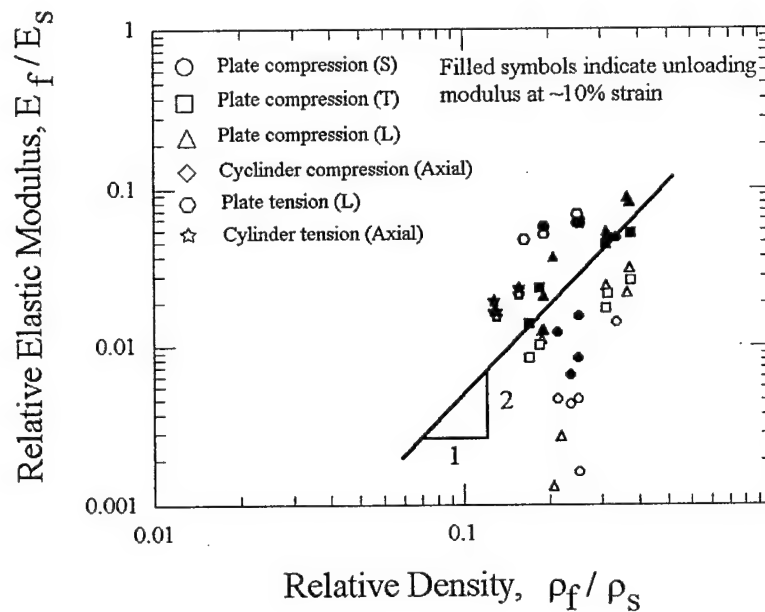
**Figure 2.4-3 Illustration of the modulus and foam strength determination from a compression  $\sigma$ - $\epsilon$  curve.**

All compression and tension test results are shown in Figure 2.4-4 where the relative strength or modulus, is plotted against relative density and the subscripts "f" and "s" refer to foam and solid, respectively. The yield strength, elastic modulus and density values for 6061-T6, 275 MPa, 69 GPa and 2.70 g/cm<sup>3</sup>, respectively, were used for property normalization. The T6 heat treatment for 6061, 18 hrs at 160°C, is similar to the T5 heat treatment used for the AMAG porous aluminum, 14 hrs at 160°C. As expected, the mechanical properties increase with relative density. The lines with slopes of 1.5 and 2 were drawn since, according to Gibson and Ashby<sup>1</sup>, the relationship between these relative parameters (strength and modulus) and density is often logarithmic with a slope from ~1.5 to 2.0 for both open and closed cell foams. In general, both the strength and modulus data show significant scatter, especially the modulus values. After ~10% strain, the compression modulus is generally higher than the initial modulus due to some consolidation of the test specimen material and due to full specimen-platen contact which may not have occurred initially. Tensile and compressive strength values are comparable, however the modulus in tension is typically greater than in compression. Interestingly, the tension data from the cylindrical specimens show comparable strength and modulus values despite the skin removal in the gage section.

<sup>1</sup> Gibson, L.J. and Ashby, M.F., Cellular Solids: Structure and properties - Second Edition Cambridge University Press, Cambridge, U.K. 1997.



(a)



(b)

**Figure 2.4-4 AMAG Al foam compression and tension test results.**

Stress calculations under 3- and 4-pt bending were computed using eqs. (2.4.4) and (2.4.5), respectively, as taken from ASTM

$$\sigma_f(3pt) = \frac{3}{2} \frac{Pl_s}{wh^2} \quad (2.4.4)$$

$$\sigma_f(4-pt) = \frac{3}{2} \frac{P(l_s - l_u)}{wh^2} \quad (2.4.5)$$

Similarly, strain computations under 3- and 4- pt bending were computed with eqs. (2.4.6) and (2.4.7), respectively, as taken from ASTM

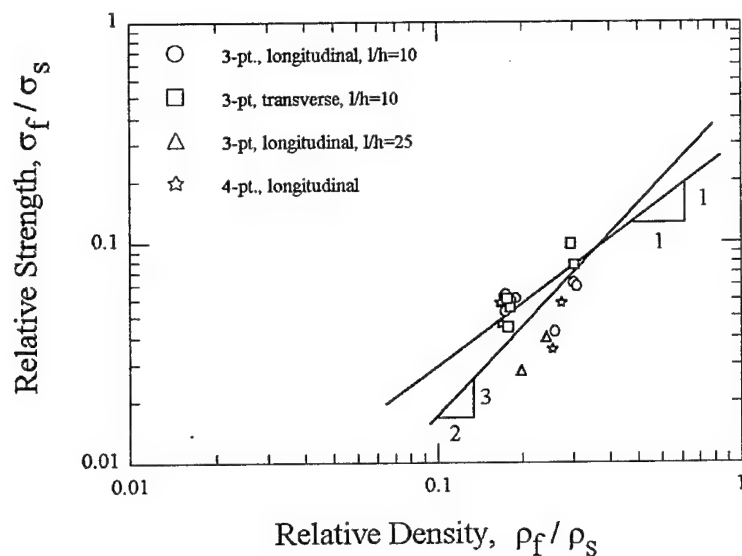
$$\epsilon_f(3-pt) = \frac{6h\delta}{l_s^2} \quad (2.4.6)$$

$$\epsilon_f(4-pt) = \frac{12h\delta}{2l_s^2 + 2l_sl_u - l_u^2} \quad (2.4.7)$$

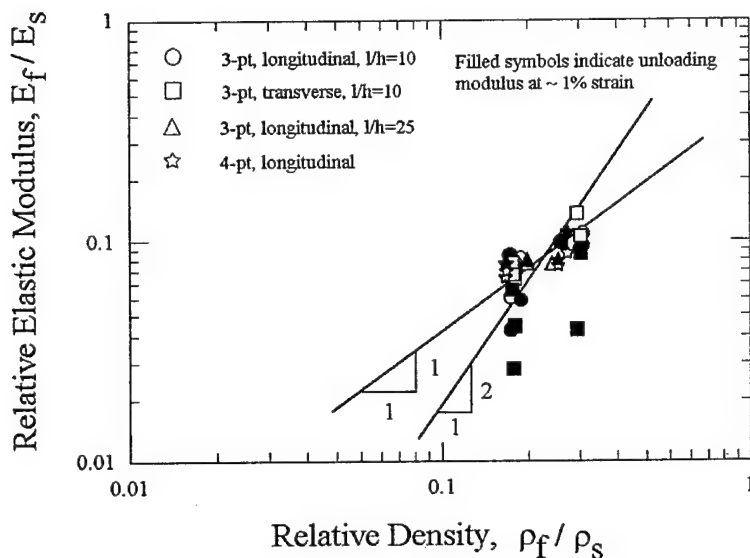
where E is computed from eq. (2.4.3).

Figure 2.4-5 shows the 3- and 4-pt bend strength and modulus results. The bend test results appear to match a line of slope 1 for both strength and modulus which Gibson and Ashby suggest a closed cell foam should, but typically does not, follow. Perhaps the skin plays a role in the different slopes observed for strength and modulus data under compression and bending. In general, the bend data under 3- and 4-pt loading do not show distinct differences discernable from data scatter, thereby suggesting that the use of the ASTM formulas for solid members is reasonable. Also, the bending modulus either remains constant or decreases after 1% strain which, contrary to the compressive modulus, increased with strain. The specimens which showed the decreasing modulus typically showed a maximum stress at less than 1% strain and contained severe deformation and/or cracks at the 1% strain level.





(a)



(b)

Figure 2.4-5 Three- and four-point bend test results.

Fatigue testing was conducted under 3-pt bending at 20Hz in air at room temperature at an R-ratio of 0.1. Results are shown in Figure 2.4-6 where failure is defined by 10mm mid-point deflection due to either progressive deformation or specimen fracture. The fatigue data are well represented by the formula

$$\sigma_{\max} = A \log(N) + B \quad (2.4.8)$$

where  $\sigma_{\max}$  is the maximum stress in the fatigue cycle,  $N$  is the number of cycles to failure and  $A$  and  $B$  are constants. The optimum values for  $A$  and  $B$  were determined for the high and low density data sets and are shown in Figure 2.4-6. The slopes of the high and low density fatigue curves quite similar, -1.93 and -2.02, respectively, but the intercepts are different, 24.4 and 17.1, respectively. It is interesting to note that even at the 5MPa maximum stress, the low density foam has not reached a fatigue limit.

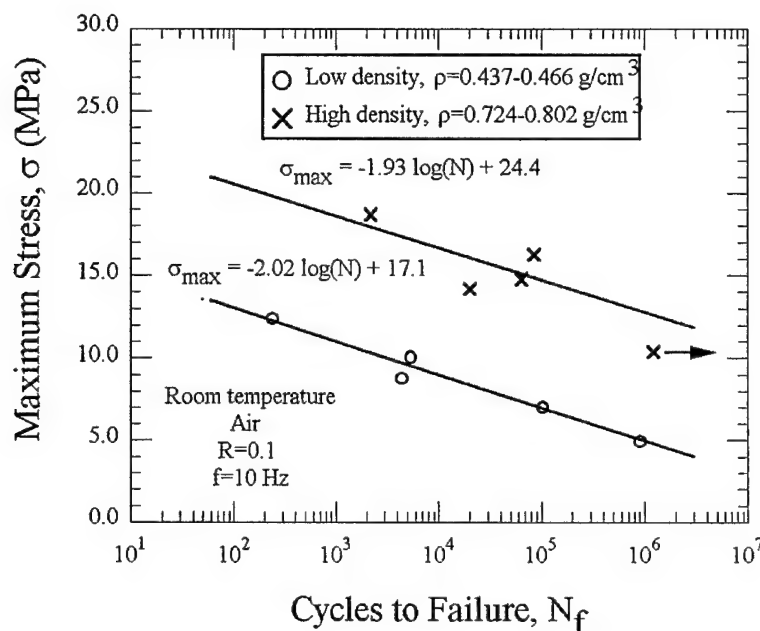


Figure 2.4-6 Three-point bend fatigue results on AMAG porous aluminum.

## 2.5 Summary

Near 6061-T6 porous aluminum plates and cylinders manufactured by AMAG have been evaluated macroscopically, microstructurally and mechanically. Macroscopically, both product forms contain a wide range of cell sizes and wall thickness combined with typical porous Al defects such as wrinkled and broken cell walls, skin thickness variations, skin ruptures and material discontinuities. Microstructurally, the material composition closely resembles 6061 with dispersed porosity and unreacted  $\text{TiH}_2$  particles. Mechanical test results indicate increasing performance with relative density although significant property variability exists. ASTM formulas for stress and strain provide a reasonable characterization of global stresses and strains under these limited test conditions.

## CHAPTER 3.0 EVALUATION OF LATTICE BLOCK MATERIAL

### 3.1 Introduction

UTRC has become aware of significant advances in the processing of 'lattice block materials', or LBM's, by Jonathan Aerospace Materials Corporation, or JAMCORP. Several years ago, JAMCORP introduced a wire bonded product with a repeatable, predictable structure. This structure was 'assembled' in a unitized fashion such that every internal node had 14 ligaments. This structure is shown in Figure 3.1-1 as taken from an aluminum alloy LBM sample.

In late 1996, JAMCORP focused on alternative approaches to low-cost manufacturing of the same structure in several different metal alloy systems in several different size scales (node to node distances of 1mm to 12mm while maintaining a nearly constant ratio of ligament diameter and node-to-node length). An aluminum LBM<sup>TM</sup> structure is shown in Figure 3.1-2 where the node-to-node distance is 12 mm (0.5 in).

The objective of this task was to evaluate the performance capability of the LBM structure, to document the structure of delivered LBM<sup>TM</sup> and to compare predictions of finite element models to properties measured on LBM<sup>TM</sup> fabricated from an aluminum alloy A356 and a nickel alloy Hastelloy-X.

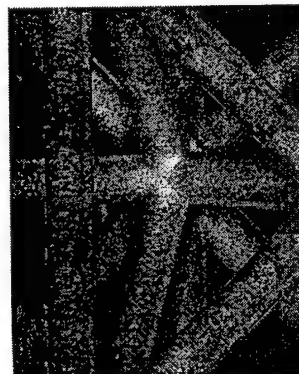


**Figure 3.1-1**      **Photograph of an Internal Node in Lattice Block Material<sup>TM</sup>**

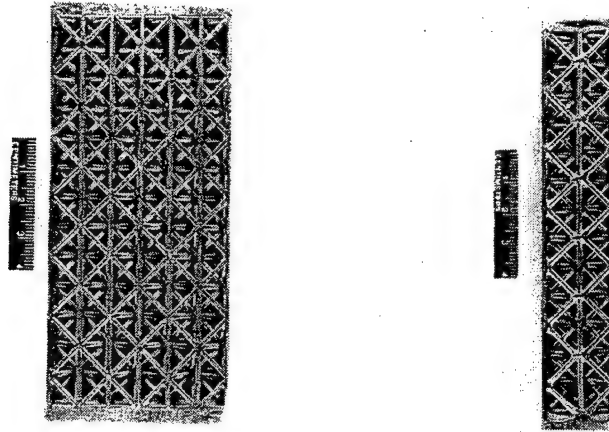


**Figure 3.1-2 Investment Cast Aluminum Lattice Block Material™ (manufactured and supplied by JAMCORP)**

Lattice Block Material™ was procured from JAMCORP (contact: Jon Priluck, President) in two material forms, A356 aluminum alloy and Hastelloy-X as summarized in the Table 3.1-1.

**TABLE 3.1-1  
LBM MATERIAL SUMMARY**

<i>Material</i>	<i>Quantity</i>	<i>Node-to-Node Distance (mm)</i>	<i>Number of Plies</i>	<i>Relative Density</i>
<i>Aluminum</i>	<i>6</i>	<i>12.7</i>	<i>2</i>	<i>12.0-12.2%</i>
<i>Aluminum</i>	<i>6</i>	<i>12.7</i>	<i>4</i>	<i>11.3-12.2%</i>
<i>Hastelloy-X</i>	<i>1</i>	<i>12.7</i>	<i>2</i>	<i>11.0-11.3%</i>

### 3.2 Macrostructural Analysis of LBM™

Overall, the lattice block material™ is a very repeatable, uniform product with essentially one measurable macroscopic variation which arises during the manufacturing process. Viewing the LBM™ structure from the through-thickness or S direction (left hand photo in Figure 3.1-2), the centerline of all ligaments appears to pass through the center of each adjoining node. In contrast, ligaments observed from the side of the structure or T direction (right hand photo in Figure 3.1-2) do not pass through the center of adjoining nodes. This is also true for ligaments observed from the end of the LBM™ block or L direction although this view is not shown.

These offsets exist throughout the entire structure and will be shown to impose a detrimental effect on the compression properties of the LBM™ in section 3.4 of this report.

The magnitude of the ligament offset was measured on 2- and 4-ply specimens along "T" and "L" faces. The surface of the specimen was ground on SiC paper, photographed to document ligament positions and then reground to the next plane of nodes for additional measurements. A total of 19 and 20 measurements were made in the "T" and "L" orientations, respectively. The average offset and standard deviation of the measurements was 1.16 and 0.035 mm, respectively along the "T" faces and 1.23 and 0.033 mm, respectively along the "L" faces. The ligament offsets tend to be independent of orientation since the average offset values are nearly equal. Similarly, the standard deviation values suggest that the scatter in offset dimensions appears independent of orientation.

### 3.3 Microstructural Analysis of LBM™

An A356 aluminum alloy LBM™ sample was sent to Dirats Laboratories (Westfield, MA) for wet chemical analysis via inductively coupled plasma emission (ICP). The chemical composition of the Hastelloy-X LBM™ was estimated via a microprobe analysis over an area about 1mm by 1mm. The results of the nominal and measured chemical compositions are summarized in Table 3.3-1. The compositions of the aluminum- and nickel-based LBM™ products are within the specifications for A356 alloy and Hastelloy-X, although the measured Mg and W contents in the A356 and Hastelloy-X samples, respectively, lie slightly below the nominal values.

TABLE 33-1  
LBM™ CHEMICAL COMPOSITIONS (WT%)

Element	A356	Aluminum LBM™	Hastelloy-X	Nickel LBM™(micro probe)
Si	7.0	6.51	0.5	
Fe	0.20 max	0.09	18.5	19.2
Cu	0.20 max	0.03		
Mn	0.10 max	<0.01	0.5	
Mg	0.3	0.22		
Zn	0.01 max	0.01		
Ti	0.20 max	0.14		
Ni		<0.01	Bal.	
Cr		0.02	22.0	22.7
Al	Bal.	Bal.		
Co			1.5	1.5
Mo			9.0	8.3
W			0.6	0.2
C			0.1	

The A356 microstructure (Figure 3.3-1) shows the typical dendritic structure of cast materials combined with a fine dispersion of Al-Si eutectic within the Al matrix and significant concentrations of interdendritic second phases. Isolated internal and surface connected porosity is observed in both the nodes and ligaments. The pores are typically 50-100 microns in size. Standard aluminum etches could not reveal grain boundaries in this material therefore grain size could not be estimated. The Hastelloy-X microstructure is shown in Figure 3.3-2 where, again, a dendritic cast microstructure is observed with interdendritic second phases. The Hastelloy-X grain size is usually over 2 mm, although the complete grain in Figure 3.3-2 is smaller than 2mm.

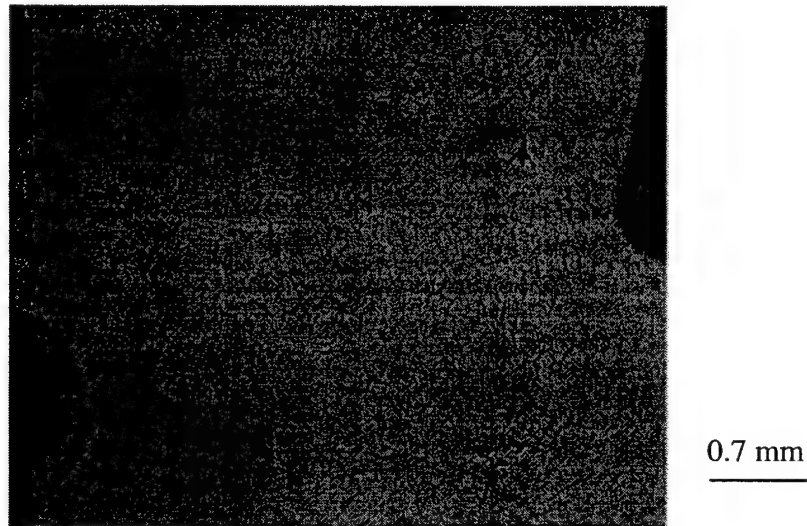


**Figure 3.3-1** Microstructure of cast A356 LBM™ showing dendritic structure with an Al-Si eutectic in an Al solution.

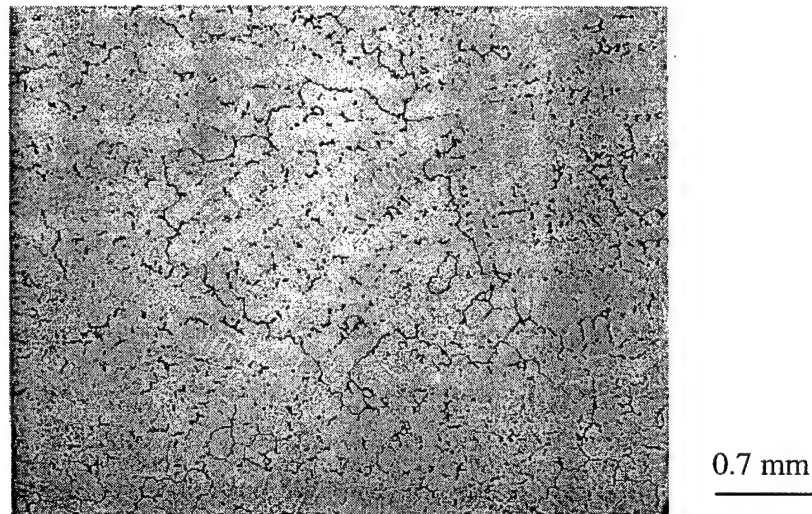


**Figure 3.3-2** Microstructure of cast Hastelloy-X LBM™ with dendritic structure and large grain size.

Microprobe analysis revealed two secondary phases in the A356 microstructure, one an Si-3.5%Al phase and the second an Al-17.2Si-23.0Fe-2.2Mn phase. In examination of polished metallographic sections, the Si-rich phase was more prevalent and varied in shape from rectangular to circular, whereas the Al-rich phase was more dispersed and was generally rectangular. Image analysis techniques were used to study the second phase area fraction in the node, in ligaments about 3mm from the node and in ligaments about half way between nodes around 6-7 mm from each node. Two LBM™ samples were sectioned and at least 30 measurements were made in each of these three areas. The average area fractions were 8.7%, 8.4% and 9.0%, in, near and away from the nodes, respectively. These numbers suggest a homogeneous distribution of alloying elements throughout the LBM™ structure.

The overall second phase area fraction in the A356 aluminum alloy LBM™ is approximately 8.7%, the average of the three area measurements. Supposing the only second phase is Si-3.5Al, its area fraction could be computed with tie lines, the lever rule and the Al-Si binary phase diagram shown in Figure 3.3-3 where only the low temperature portion of this diagram is shown for simplicity. Si and Al are nearly insoluble in the solid phase at room temperature therefore pure metal densities are used to convert 6.5wt% Si in an Al-Si alloy to an equivalent vol%, 7.5%. The other second phase, the Al-rich particles, accounts for the additional area fraction observed from image analysis. However, the area fraction of this phase is more than 1.0% (8.7%-7.5%) since this Al phase consumes some the Si which was used to calculate the 7.5% number. No quantitative evaluations were performed to determine the relative proportions of Si-Al and Al-17.2Si-23.0Fe-2.2Mn, although qualitatively, the Al-Si phase appears more prevalent.

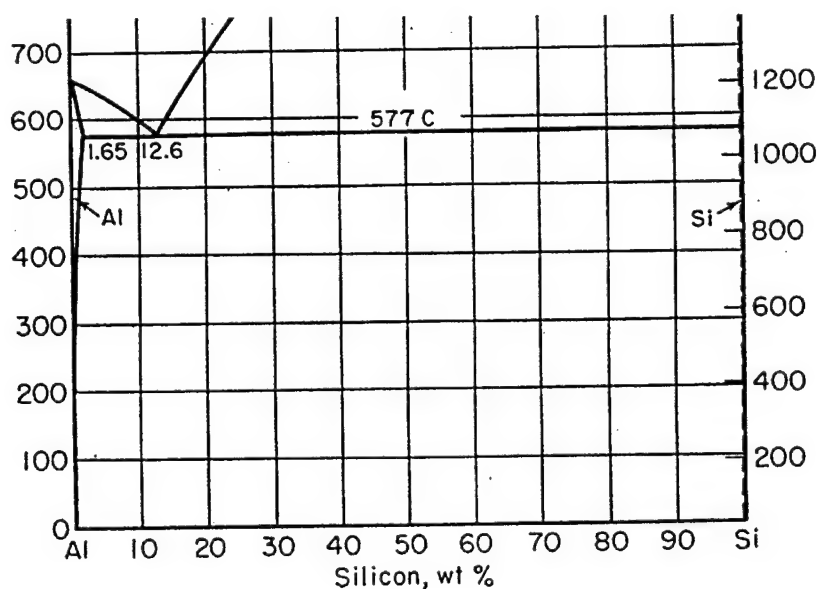
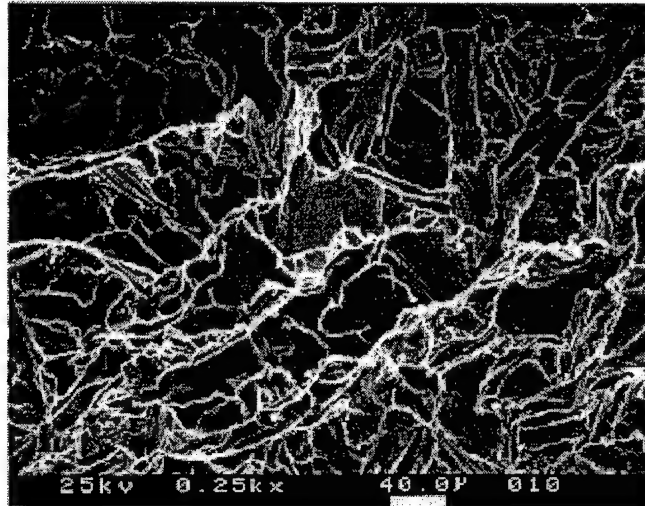
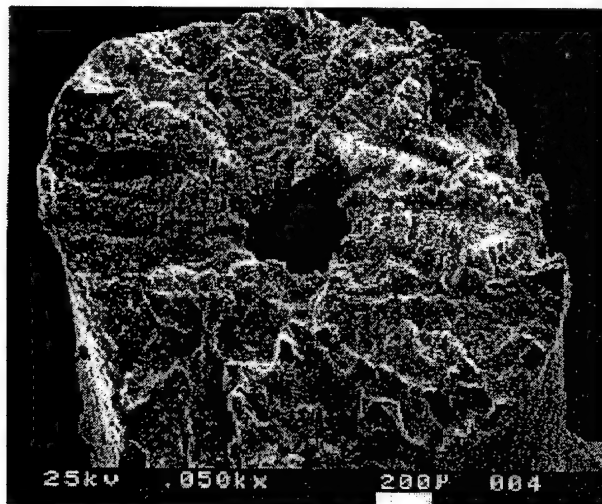


Figure 3.3-3 Al-Si binary phase diagram. (Extracted from Aluminum: Vol. 1. Properties, Physical Metallurgy and Phase Diagrams, ASM, 1967)

Several A356 tensile specimens were machined from the solid 'over-cast' end plates shown at the top and bottom of the LBM™ block in Figure 3.1-2. The fracture surfaces of these tensile specimens indicated a brittle transgranular crack propagation mode with occasional evidence of initial casting porosity as shown in Figure 3.3-3. Hastelloy-X fractographs were taken from individual ligaments which failed due to bending and limited torsion during compression tests of the LBM™ structure. Figures 3.3-4 and 3.3-5 illustrate the intergranular and interdendritic fracture path in the cast Hastelloy-X material.



**Figure 3.3-3** Fracture surface of tensile specimen fabricated from A356 LBM.



**Figure 3.3-4** Fracture surface of Hastelloy-X ligament with a macroscopic internal void.



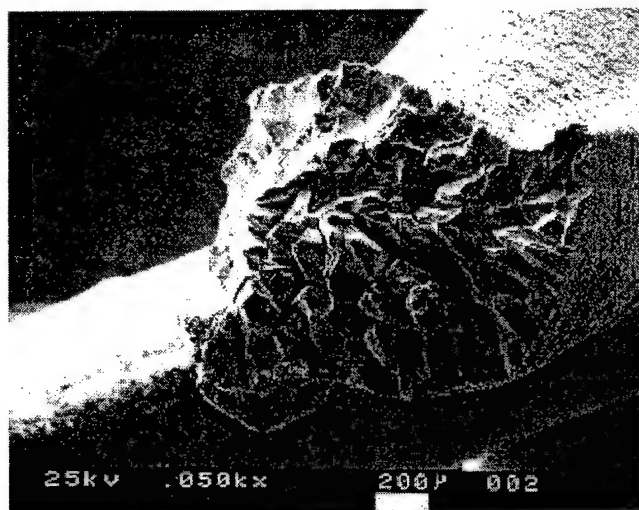


**Figure 3.3-5 Fracture surface of Hastelloy-X LBM™ ligament.**

### **3.4 Structural Evaluation of Lattice Block Material™**

In evaluation of the mechanical performance, investment cast aluminum and Hastelloy-X LBM™ material were selectively tested in compression (17 tests) and 3-pt. bending (2 tests). All testing was performed at room temperature in laboratory air on a Tinius Olsen testing machine with force measured by a load cell and specimen deflection measured by a deflectometer. The crosshead displacement rate was maintained at 2.54 mm/min for both the compression and bend experiments. Prior to every compression test, a thin (75  $\mu$ m) sheet of soft, high-purity aluminum was placed between the sample and load platens to reduce anomalous data collection resulting from an initial lack of complete specimen-platen contact. The 3-pt bend specimens were contacted with plates measuring 9.5mm wide and either 3.3mm or 0.5 mm thick for load application. The lower span,  $l_s$ , to height,  $h$ , ratio on the 3-pt bend tests was limited to, and maintained at, 4. For each specimen, load-displacement curves were traced on an X-Y recorder and standard ASTM equations (2.4.1, 2.4.2, 2.4.3, 2.4.4 and 2.4.6) were used to convert the load-displacement results to stress and strain.

Figure 3.4-1 shows several stress-strain curves generated from compression tests on A356 and Hastelloy-X 2-ply LBM™ samples. Comparing the A356 and Hastelloy-X test results indicates that, under a given testing orientation, the Hastelloy-X samples withstood a higher peak stress value. The enhanced load capability is attributed to the higher ultimate strength of Hastelloy-X since the yield strengths of the materials are similar, 220 and 260 MPa for A356 and Hastelloy-X, respectively. Second, the strain at peak stress is slightly larger for the Hastelloy-X samples, probably due to the fact that the ultimate strength of Hastelloy-X occurs at a higher strain level than for A356. Third, after maximum sample stress is reached, the load bearing capacity of the A356 samples decreases significantly faster than for the Hastelloy-X material. Due to the limited tensile ductility of the aluminum alloy, about 2.4%, many ligaments fracture at

the peak stress condition whereas the Hastelloy-X ligaments generally continued to bend, an ability provided by higher tensile ductility, about 41%. Parent metal ductility also appears to explain the relatively higher stress values in the "valley" of the stress-strain traces since most of the aluminum ligaments have broken and are unable to sustain load.

An orientation effect is also observed from Figure 3.4-1 whereby loading in the "L" direction consistently supports greater load, likely due to the alignment of some ligaments in the L direction and no ligaments parallel to the S and T directions, as seen in Figure 3.1-2. All orientations show evidence of an initial stress peak and a stress valley followed by one or more peaks and valleys. During compression, a plane of ligaments within the LBM™ structure often fails producing a decrease in load support. The additional stress increases arise from the compression platens contacting a relatively undeformed plane of material. Second and third stress peaks did not reach the initial peak suggesting some damage has been incurred by the LBM™ structure at the initial peak. Another orientation effect appears to be that the S and T samples drop to lower stress values in the valleys than the L specimens, especially those fabricated from A356. The ligament offset discussed in section 3.3 seems to play a role in this observation since, especially in the T direction, a macroscopic shear band extends through the entire sample as illustrated in Figure 3.4-2. Ligaments in the lower left and upper right hand corners of the sample remain nearly undamaged whereas material in a band stretching from the upper left to lower right hand corner of the specimen has undergone severe deformation.

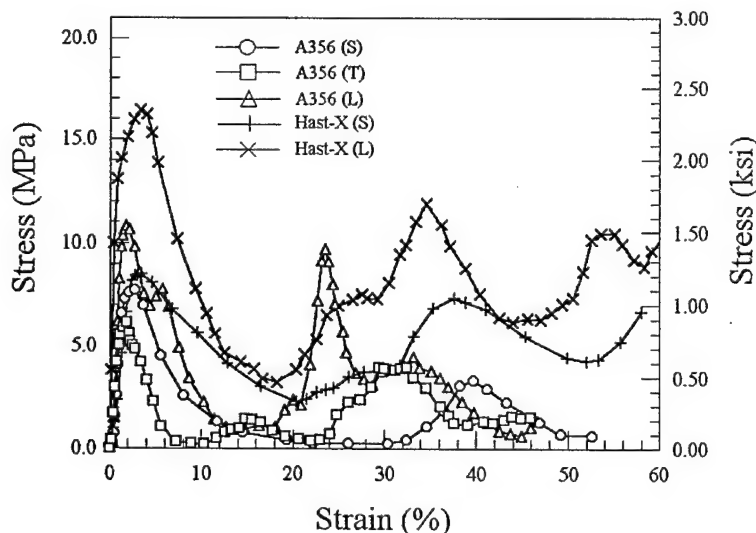
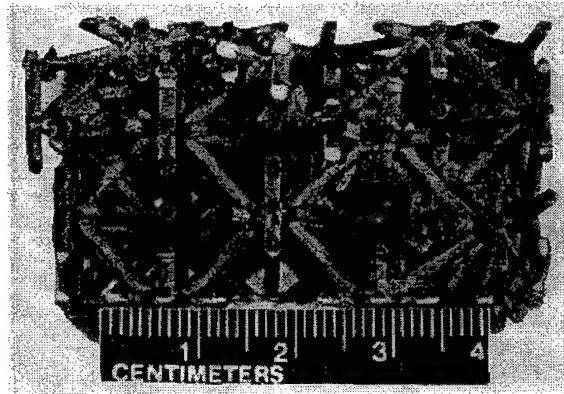


Figure 3.4-1 Compression stress-strain curves for 2-ply LBM samples.



**Figure 3.4-2 Deformed A356 LBM compressed in the T direction.**

Figure 3.4-3 compares the LBM<sup>TM</sup> compression and bend strength to the AMAG porous aluminum compression strength with all data normalized by the 0.2% yield strength of the parent metal and the specimen density normalized by the parent metal density. Both the aluminum and nickel alloy LBM's show superior compression results, because of the average relative strength lies approximately four times higher than the AMAG porous aluminum and the LBM<sup>TM</sup> data points show significantly less scatter, even when two parent metals are included in the comparison.

It should also be noted that the bending strength data points from A356 aluminum LBM<sup>TM</sup> samples fall nearly 4 times higher than the compression strength points. This effect may be inherent to the LBM<sup>TM</sup> configuration or may be an artifact of using ASTM formulas for stress computations that were derived for solid test specimens.

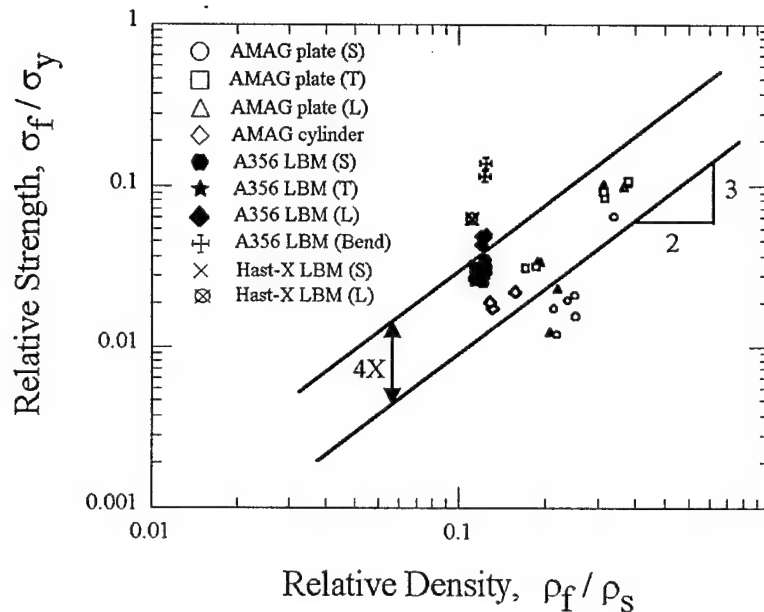


**Figure 3.4-3 Comparison of AMAG Porous Aluminum and A356 LBM<sup>TM</sup> Strength**

Figure 3.4-4 shows the experimental elastic modulus data obtained from compressing and 3-pt bending LBM<sup>TM</sup> samples and AMAG porous aluminum. The average LBM<sup>TM</sup> and AMAG foam stiffness results are comparable, however as with the strength data, less data scatter seems to be associated with the LBM<sup>TM</sup> results. There is no clear explanation for the low modulus of the Hastelloy-X specimen compressed in the S direction. The relative LBM<sup>TM</sup> 3-pt bending stiffness is greater than the relative LBM<sup>TM</sup> compression stiffness. Again, this effect may be inherent to the LBM<sup>TM</sup> configuration or may be an artifact of using ASTM formulas for stress and strain computations that were derived for solid test specimens.

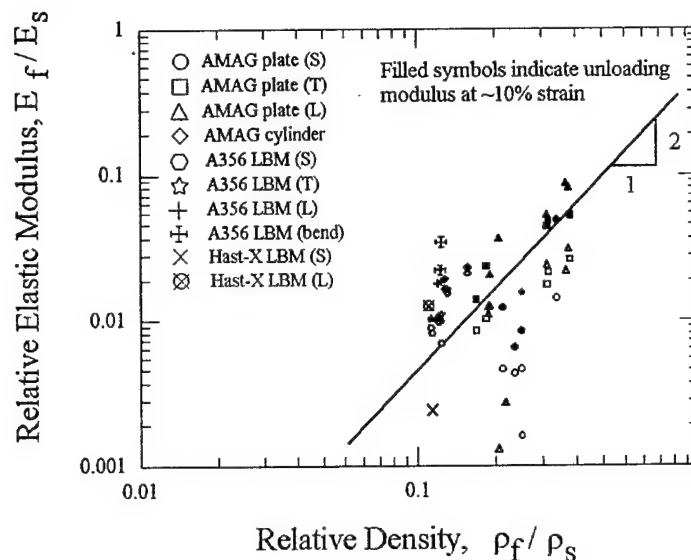
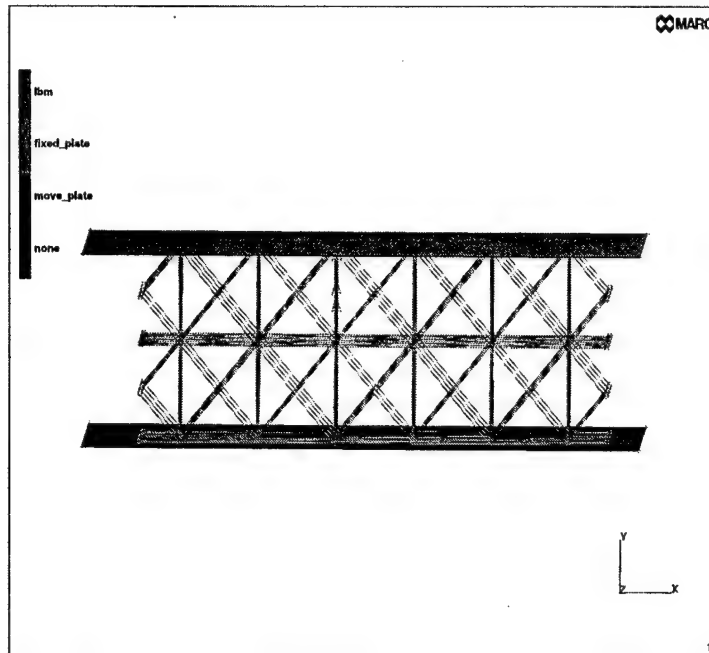


Figure 3.4-4 Comparison of AMAG Porous Aluminum and A356 LBM™ Modulus.

### 3.5 Finite Element Modeling of Lattice Block Material™

Finite element analysis was initially used to simulate the mechanical testing observations reported in section 3.4 and then to assess the effects of unit cell size (node-to-node variation), ply number (1,2 or 4) and parent material properties (investment cast aluminum, steel and nickel alloys) on structural performance.

The finite element model was built using Mentat II 2.3.1 and solved with MARC Ver. 6.2, both running on a Silicon Graphics workstation. Each ligament in the LBM™ structure was modeled as a single beam element with 7 degrees of freedom, 3 displacements ( $u$ ,  $v$ ,  $w$ ), 3 rotations ( $\theta_x$ ,  $\theta_y$ ,  $\theta_z$ ) and axial strain ( $d\bar{u} / ds$ ) which is MARC element #25. Compression tests were simulated by an LBM™ placed between two rigid surfaces, one of which is fixed and the other movable. To prevent the LBM™ block from sliding out from between the surfaces, an additional boundary condition is imposed. One node which contacts the fixed surface and is near the center of the structure is prevented from translating in either direction perpendicular to the plane of the fixed surface. Sample compression is initiated by bringing the movable surface in contact with the LBM™, then translating the moving plate towards the fixed plate at a constant velocity. The predicted LBM™ response is essentially independent of this displacement rate since no material rate effects are built into the model. However, the rate must be slow enough to achieve a model solution at each time interval. The total force supported by the LBM™ structure is the measured by the force applied to either surface and the displacement is measured by the movement of the movable surface. The through-thickness (S) compression model of a 2-ply LBM™ sample is shown in Figure 3.5-1.



**Figure 3.5-1 FEM of through-thickness (S) compression test on LBM™ sample.**

For plastic deformation predictions, a uniaxial stress versus plastic strain curve is required. For the A356 alloy, tensile data was determined from three tensile specimens (Figure 3.5-2) machined from the 'over-cast' material shown on the ends of the block in Figure 3.1-2 to determine, as closely as possible, the parent alloy properties. The elastic moduli, 0.2% yield strength and ultimate strengths of the three samples were quite similar, 58.6-73.8 GPa, 209-226 MPa and 231-260 MPa, respectively, however one failure strain, 0.7%, was significantly less than the other two 2.2% and 2.6%. No significant differences were observed on the fracture surfaces of the three samples using optical and SEM analyses. The stress-strain curve used in the FEM for A356 is shown in Figure 3.5-3 along with the experimental data. Yield strength, tensile strength and elongation data (261 MPa, 530 MPa and 41%, respectively) for the Hastelloy-X material were provided by the casting vendor, Komtek (Worcester, MA). Using the handbook elastic modulus value of 197 GPa, an approximate stress-strain curve for Hastelloy-X was constructed for the finite element model.

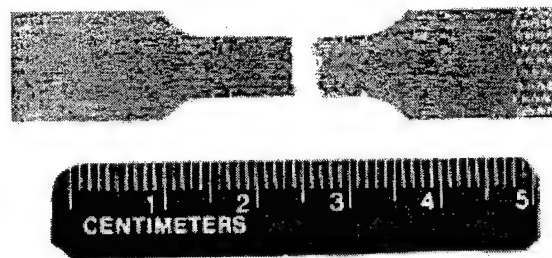


Figure 3.5-2 Tensile specimen used to determine A356 stress strain curve.

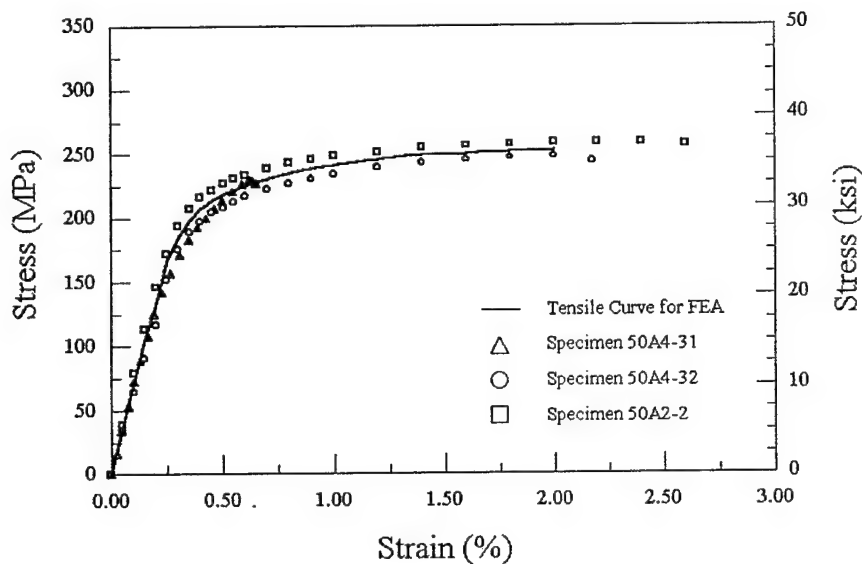
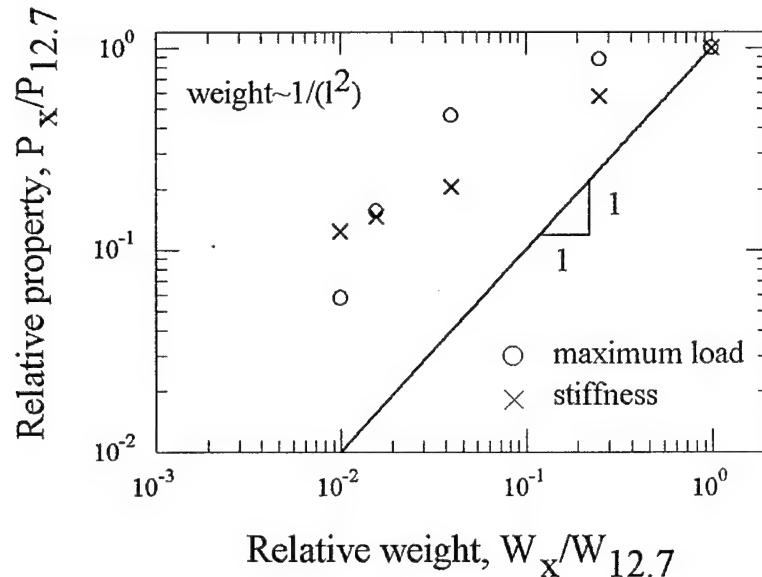


Figure 3.5-3 A356 Tensile stress-strain curves.

Finite element predictions for both compression and bending of LBM<sup>TM</sup> compare well with experimental data. Under compression loading, 2- and 4-ply predicted strength values were within typically within 25% but the predicted modulus was generally higher than the experimental modulus, by as much as a factor of 2. The predicted 3-pt bend strength and stiffness were within 15% and 50%, respectively. No clear explanation is apparent for the higher moduli under both compression and bending. Perhaps incomplete contact existed between the LBM test specimens and loading plates during experimental testing thereby reducing the measured specimen modulus.

Through-thickness (S) compression of the A356 2-ply specimen was selected to investigate the effect of unit cell size (weight), ligament diameter (weight) and parent metal ultimate strength on LBM<sup>TM</sup> structural response. The unit cell size effect on mechanical performance is illustrated in Figure 3.5-4 where the predicted capability and LBM<sup>TM</sup> weight are normalized by the predicted properties and actual weight of the 12.7mm spacing LBM<sup>TM</sup>. To a first approximation the weight scales with the unit cell size, or ligament length, as  $w \propto 1/l^2$ . Points lying above the

line with a slope of 1 suggest a possible property to weight ratio gain since cutting the LBM™ weight in half reduces the mechanical properties less than 50%. However, the actual variation of LBM™ weight with unit cell size should be established with LBM™ manufactured from a variety of node-to-node spacings.



**Figure 3.5-4 FEA predictions for the effect of unit cell size on the 2-ply through thickness strength and stiffness of A356 aluminum alloy LBM™.**

To a first approximation, product weight altered by ligament diameter and strength vary linearly as shown in Figure 3.5-5, where the FEA predictions are normalized by the predicted properties and weight of the actual A356 LBM™ with 1.5mm diameter ligaments. Deviations from linearity are only predicted for LBM™ constructed from high aspect ratio (length to diameter) ligaments.

Likewise, a linear relationship is predicted between LBM™ strength and parent metal ultimate strength as shown in Figure 3.5-6. These predictions were obtained by estimating the uniaxial stress-strain curve for higher strength materials from modulus, yield strength and ultimate strength handbook data.



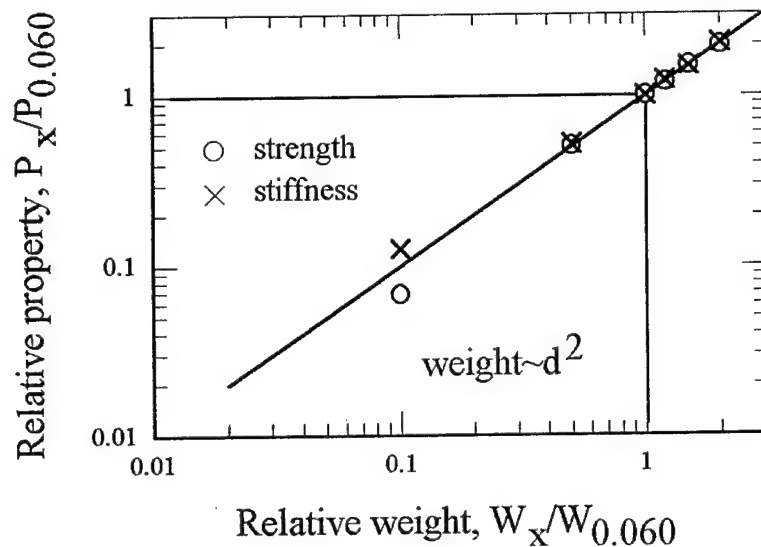


Figure 3.5-5 FEA predictions for the effect of ligament diameter (weight) on the 2-ply through thickness strength and stiffness of A356 aluminum alloy LBM<sup>TM</sup>.

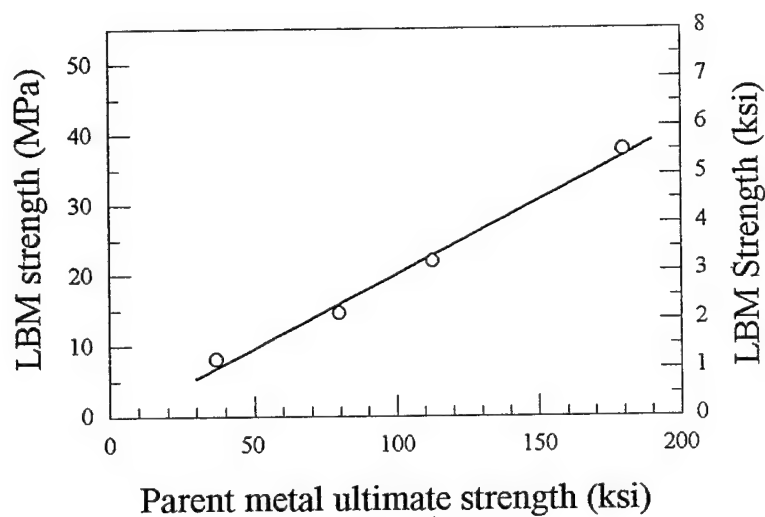


Figure 3.5-6 FEA predictions for the effect of parent metal ultimate strength on the 2-ply through-thickness compression strength of LBM<sup>TM</sup>.

### 3.6 Summary

Lattice Block Material (LBM™) has been evaluated macroscopically, microstructurally and mechanically. Macroscopically, the structure shows exceptional uniformity although ligament-to-node offsets, which appear to have a detrimental effect on mechanical properties, are apparent in two dimensions. Microstructurally, both the A356 and Hastelloy-X samples have a dendritic, cast structure with varying degrees of porosity. Small dispersed porosity is evident in the aluminum alloy whereas gross porosity has been identified in the Hastelloy-X ligaments. Mechanically, the LBM™ shows superior strength and comparable stiffness to AMAG porous aluminum under compression loading. Also, repeated LBM™ compression tests show excellent repeatability. LBM™ strength and stiffness are superior under 3-pt. bending than under compression testing, perhaps due to the LBM™ geometry or perhaps due to the use of stress formulas derived for solid test specimens. Finite element model predictions show reasonable agreement with experimental results and suggest that LBM™ performance scales linearly with both parent metal ultimate strength and structural weight. A potential strength to weight ratio benefit exists with a limited increase (up to ~8X) in cell size.

## 4.0 CONCLUSIONS

### AMAG Porous Aluminum

- Both the plate and cylinder product forms contain a wide range of cell sizes and wall thicknesses. Typical SPM defects are observed such as wrinkled and broken cell walls, cell wall porosity and skin thickness variations.
- The chemical composition closely matches typical aluminum alloy 6061.
- The microstructure consists of an Al-Si-Mg matrix with dispersed porosity and unreacted  $\text{TiH}_2$  particles surrounded by an Al-Ti-Si-Mg phase.
- Mechanical property data shows significant scatter and follows trends predicted by Gibson and Ashby.
- Mechanical test results from plate and cylinder specimens show no distinct differences discernable from data scatter associated with a single product form.
- ASTM formulas provide a reasonable characterization of global stresses and strains under the conditions studied, compression, tension and 3- and 4-pt bending.
- S-N fatigue curves generated on high and low density specimens under 3-pt bend loading have similar slopes with different intercepts.

### JAMCORP Lattice Block Material (LBM™)

- The LBM™ structure shows exceptional uniformity with slight ligament - node offsets.
- Both the A356 and Hastelloy-X microstructures are dendritic with interdendritic second phases. Limited porosity was observed in both parent metal products although the large porosity was found in the Hastelloy-X ligaments.
- Mechanical test data are very repeatable and are comparable or superior to the AMAG foam in terms of stiffness and strength, respectively.
- Finite element modeling shows reasonable agreement with experimental test data. Predictions indicate that LBM™ strength varies linearly with weight and the ultimate strength of the parent metal.

## 5.0 ACKNOWLEDGEMENTS

This work has been supported by the Office of Naval Research with Dr. Steven G. Fishman as the contract monitor. Dr. Fishman's support and guidance throughout this program is greatly appreciated. The assistance provided by UTRC's Materials Characterization group is acknowledged for the metallurgical results, phase analysis and image analysis work. UTRC's Materials Testing group is also recognized for the mechanical test results. The help provided by Dr. Pradipta Sarkar of UTRC's Quality Systems group with the ANOVA is also appreciated.

## APPENDIX A

The original contract N00014-95-C-0231, Evaluation of Structural Porous Metals, was approved on 11 May 1995. Work from contract initiation through the 1 May 1997 is summarized this Appendix.

A modified technical statement of work for this program was submitted to ONR on 3 April 1997. The body of this final report summarizes the work performed under this modified work statement. The motivations for redirecting the work were: (i) process difficulties noted here, and (ii) changes in vendor capability.

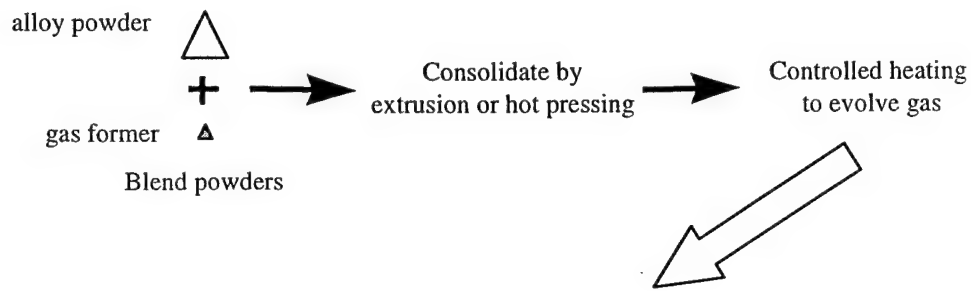
---

---

### ALUMINUM SPM CONCEPT EVALUATION

#### A.1 Objective

The objective of this task was to manufacture a 2000 series aluminum structural porous metal (SPM) for characterization of structure and mechanical properties. The manufacturing process is based on powder blending, extrusion processing and a heat treatment cycle as illustrated in Figure A.1-1.



Structural Porous Aluminum

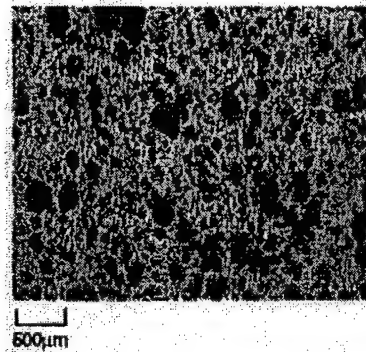


Figure A.1-1 Manufacturing process schematic

The first task of the activity was to demonstrate the capability to create 2124 aluminum foam using both the  $\text{TiH}_2$  and  $\text{CaCO}_3$  SPM foaming agents. Procedures followed those successfully demonstrated for 6061 aluminum (N00014-95-C-0148, Evaluation of Aluminum Metal Foam). An optimized process would provide improved pore structure control on the 2124 aluminum SPM resulting in greater reliability and reproducibility of performance.

### A.2 Extruded Precursor Fabrication

The materials are summarized in Table A.2-1.

**TABLE A.2-1**  
**MATERIAL SUMMARY**

<u>Extrusion #</u>	<u>Foaming Agent</u>	<u>Container Matl/ Dia. (mm)</u>	<u>Degas Temp (°C) and Time (min)</u>	<u>Extrusion Temp (°C)</u>	<u>Final Rod Dia. (mm)</u>
2124-1 (UTF-6)	2 wt% $\text{TiH}_2$	Al/51	496 °C/60 min	482 °C	15.9
2124-2 (UTF-11)	2 wt% $\text{CaCO}_3$	Al/51	496 °C/60 min	482 °C	15.9
2124-3 (UTF-12)	4 wt% $\text{CaCO}_3$	Al/51	496 °C/60 min	482 °C	15.9
2124-4 (F13)	1 wt% $\text{TiH}_2$	Al/51	496 °C/60 min	482 °C	18
2124-5 (F14)	2 wt% $\text{TiH}_2$	Al/51	496 °C/60 min	482 °C	18
2124-6 (F15)	4 wt% $\text{TiH}_2$	Al/51	496 °C/60 min	482 °C	18

### A.3 Processing of SPM

#### A.3.1 Introduction

A general description of UTRC's SPM post-processing follows. A measured mass of extrusion is placed in a thin-walled steel tool. Thermocouples are fixed to the tool and the part is placed into an air furnace set at 800 °C (1472 °F). The thermocouples are used to monitor the progress of foaming. The surface temperature of the steel tool drops when the additional thermal mass of the foam contacts the tool. At the first indication of a drop in tool surface temperature (typically 3-4 minutes into the heating exposure period), the tool and sample are removed from the furnace and quenched in water.

A series of experiments were performed to determine the effect of several material variables and process variables on SPM quality. Emphasis was placed on understanding the effects of precursor composition, thermocouple/tool configuration and presence of billet casing on the SPM samples.

#### A.3.2 Process Control via Temperature Monitoring

Thermocouple location was critical to accurately monitor the SPM foaming process. A series of experiments were performed to evaluate the sensitivity of processing to thermocouple location. The experimental set up is shown schematically in Figure A.3.2-1.

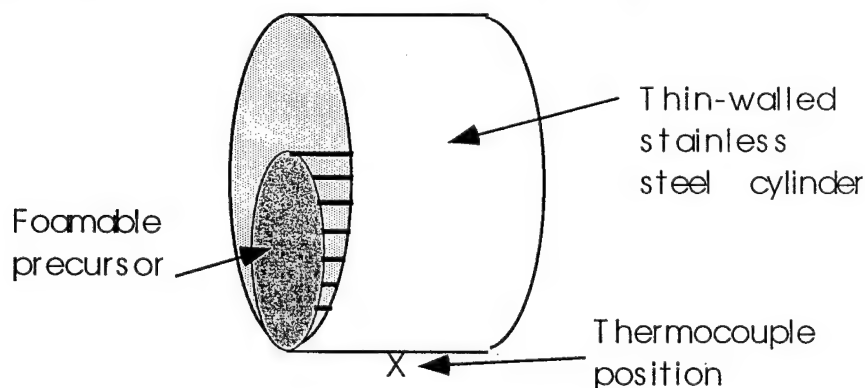


**Figure A.3.2-1 Tool configuration for foaming experiments**

It was determined that the presence of and condition of the billet material casing over the foamable precursor had a significant effect on the foaming process and the product quality. If the casing is completely removed prior to the foaming heat treatment the thermal response shows a single local minimum (i.e., a dip). Whereas if the casing remains on the extrusion, the thermal response shows at least two local minimum (i.e., a double-dip). This effect is described in greater detail below.



Other trends have also been noted:

#### **Thermocouple and tool contact**

Tests demonstrated that the degree of thermal contact between the thermocouple and tooling is important. Variability of this contact adversely influences reliability of the temperature/time monitoring. As the thermal contact degrades, the thermocouple reading appears to lag the actual temperature of the extrusion/tool assembly.

#### **Thickness of the tool wall**

A thicker walled tool showed a larger drop in temperature at the onset of foaming.

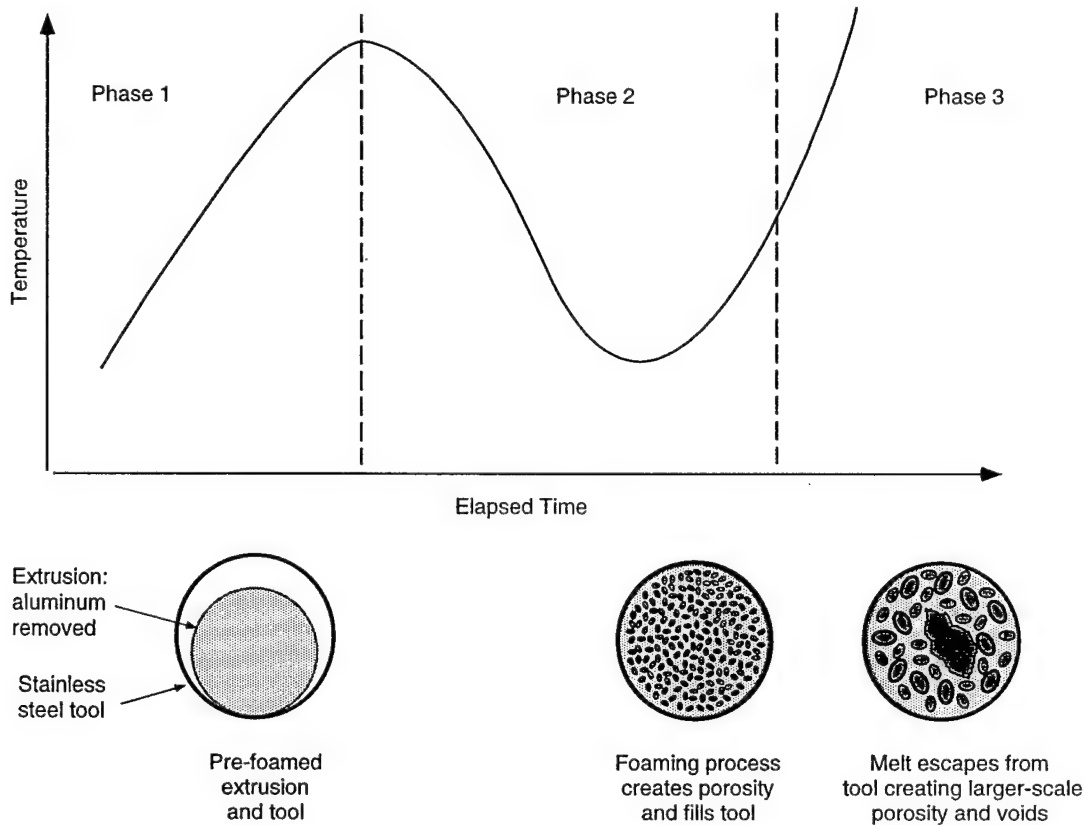
#### **Volume of the tool**

For a given extrusion (foaming agent chemistry and concentration), there was a limit to the gas volume that can be released and the level of porosity that can be developed. As lower density, higher porosity parts are being considered, conditions can develop where the foaming metal will not fill the tool. Therefore, the thermocouple may not show a drop in temperature.

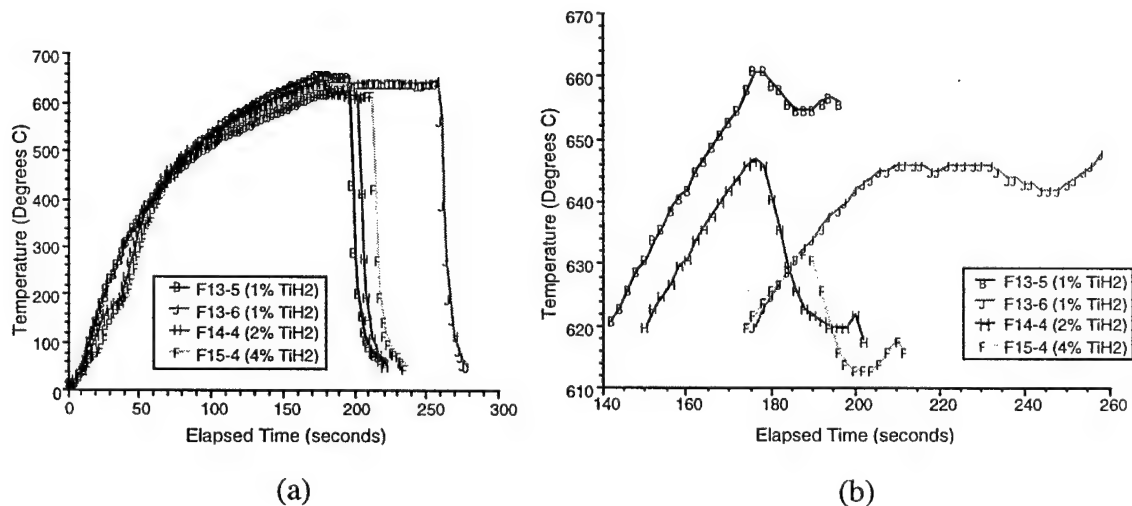
#### **A.3.3 Aluminum billet casing removed from extrusion.**

Figure A.3.3-1 shows typical qualitative features of a temperature-time profile for the case in which the aluminum surface has been removed from the extrusion. At the bottom of the figure, representations of the pore structure for progressive phases of the foaming process are shown. It is clear from the relationship between the temperature time profile and the pictorial foam representations that the timing of the quench stage is critical to consistent and repeatable foam structure and properties.

Figures A.3.3-2 show actual temperature-time profiles for a series of typical foaming runs. The precursor extrusion cylinders were quite similar in size. However, some profiles differ significantly both in maximum temperature reached before the onset of the "temperature dip" and/or the time-span over which this onset occurs. Although intrinsic differences in the precursors containing varying percentage of  $\text{TiH}_2$  may account for some of these differences, variation in the thermal flow patterns influenced by thermocouple-to-tool contact and tool-to-sample contact, most likely account for the majority of them. For instance, test samples F13-5 and F13-6 differ markedly in the time-span over which the characteristic temperature dip occurs. Cross-sections of these same samples indicate that the temperature dip occurred much further along in the foaming process for F13-6 than for F13-5. Differences such as these indicate significant differences in thermal contact and thermal flow characteristics in the two cases. F13-6 most likely had poorer contact and heat flow characteristics than did the other three samples.



**Figure A.3.3-1** Qualitative features of temperature/time profile and its relationship to structural changes in the foaming product at each stage. (aluminum extrusion can removed.)



**Figure A.3.3-2** Temperature/time profiles for  $\text{TiH}_2$  - 2124 aluminum test foaming runs with aluminum casing removed.

#### A.3.4 Aluminum billet casing surrounds extrusion.

When an aluminum casing surrounds the precursor, the foaming process becomes more complicated than described above. The surface appears to act as a ring structure, constraining the expansion. In this case, the temperature-time profile will tend to exhibit a "double-dip" effect as shown in Figure A.3.4-1. The first temperature decrease is apparently associated with rupture of the aluminum ring and the second associated with the actual foaming/melting of the extrusion precursor.

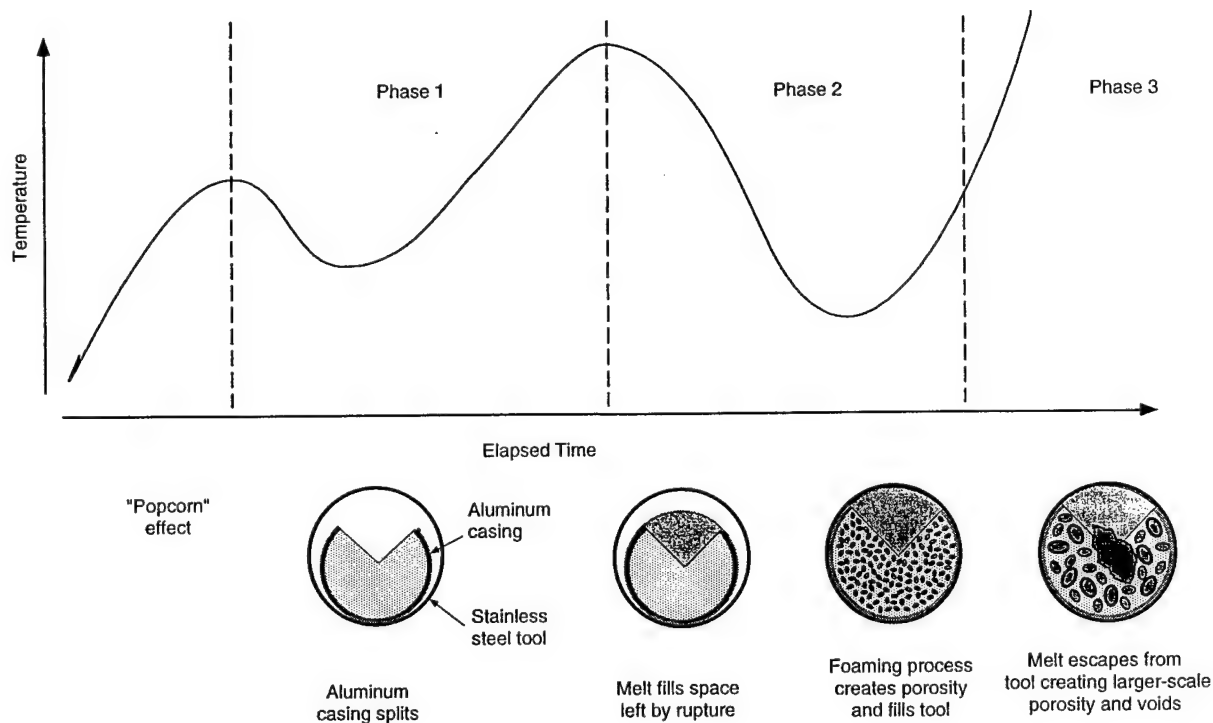
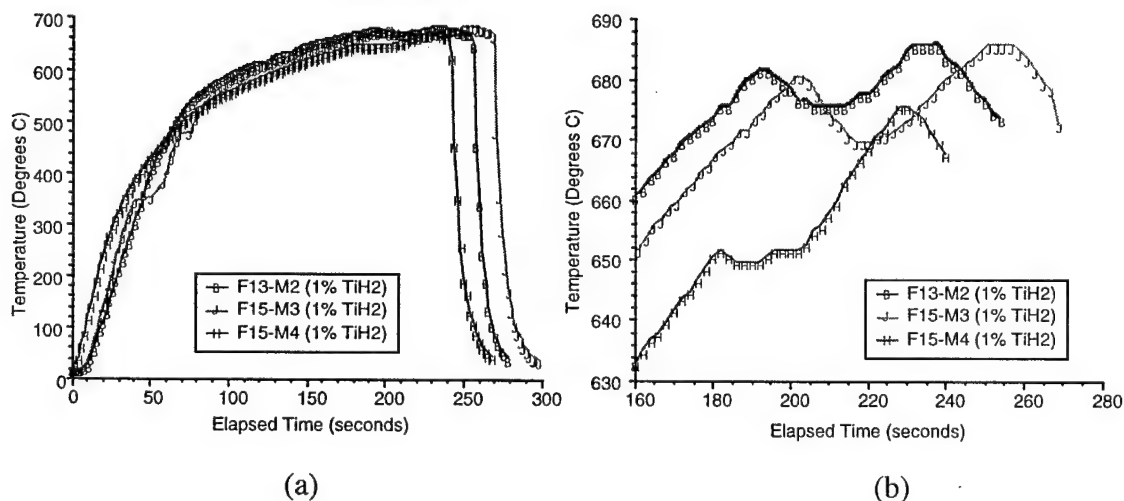


**Figure A.3.4-1** Qualitative features of temperature/time profile and its relationship to structural changes in the foaming product at each stage. (case for aluminum surface).

When a cold sample is placed in a pre-heated furnace, the interior of the extrusion will always be cooler than the outer portion of the extrusion and the stainless steel containment tool. When the aluminum ring ruptures, which may occur in one or several places around the perimeter of the ring, the cooler interior of the extrusion is exposed to the hotter containment cylinder. As heat is transferred to the interior of the extrusion in response to this change, the monitoring thermocouple temperature at the bottom of the containment cylinder shows either an inflection in the temperature/time profile or an actual dip depending on the severity of the effect described above as shown in Phase 1 of Figure A.3.4-1.

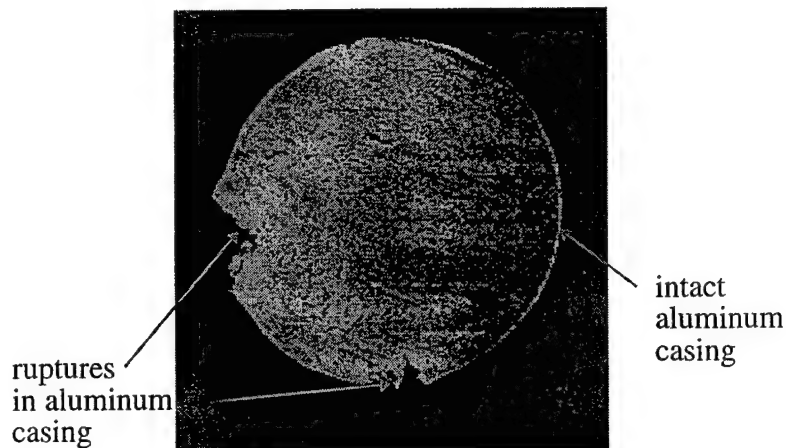
The temperature decrease in Phase 2 is related to a more controlled generation of porosity. This is equivalent to the thermocouple response observed in the 'single' dip profile with no casing.

Figure A.3.4-2 shows temperature-time profiles for a series of typical foaming runs. Notice the characteristic "double-dip" for two of the three profiles. Note that the severity of the temperature dip differs for test samples F15-M3 and F15-M4. Heat flow factors similar to those discussed above where the aluminum casing was removed from the precursor are also important for this more complex situation. However, the thickness of the aluminum casing is also a likely contributing factor. Suppose now that a controlled experiment were carried out in which only the thickness of the aluminum casing were allowed to vary. In this case, one would expect to start with a substantial temperature dip with aluminum casing present. The dip would be expected to gradually recede with removal of the casing, ending with no discernible dip when the casing had been completely removed.



**Figure A.3.4-2** Temperature/time profiles for test foaming runs with aluminum casing partially intact.

A sample cross-section for a typical foaming runs for which an aluminum casing was present are shown in Figure A.3.4-3. The most significant difference between these foaming runs and those shown above without the aluminum casing is the presence of a region of little or no porosity at the perimeter of the test samples.



**Figure A.3.4-3** Axial cross-section of typical sample for which an aluminum casing was at least partially intact and quench preceded melting. (Mag: 2X)

#### A.4 Structural Characterization

General macrostructural evaluation was performed to support the foaming studies reported above.

Microstructural characterization has generally shown a broad distribution of the pore volume and shape as adequate process control has not yet been defined. Figure A.4-1 shows representative foam sections produced from 1%  $\text{TiH}_2$  (F13-M1, F13-M2) and 2%  $\text{TiH}_2$  (F14-M8, F14-M9) in aluminum 2124 precursors. A wide distribution in pore structure is clearly evident and, as will be shown below, leads to extensive scatter in the compression test data.

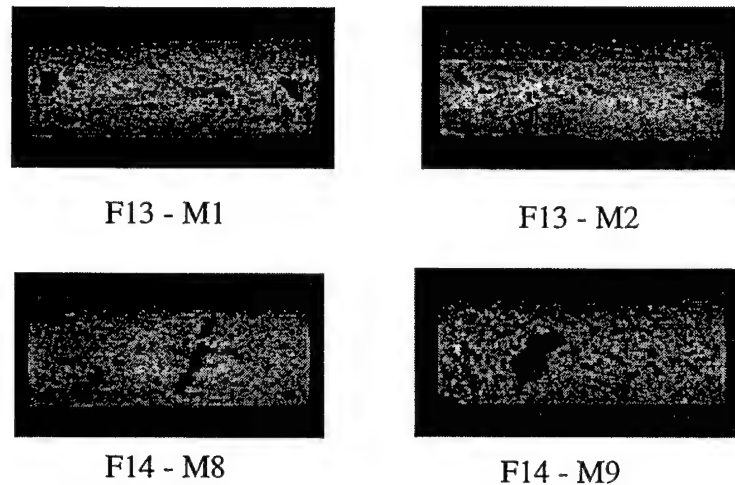


**Figure A.4-1**      **Representative photos showing porosity structure for TiH<sub>2</sub>-2124 Aluminum test samples. (Mag: 1.5X)**

## **A.5 Property Measurement**

### **A.5.1 Density/compositional relationships**

Values for both measured and theoretical densities were compared for the three extrusion compositions. The theoretical densities were computed by the rule-of-mixtures using handbook values for the densities of Al 2124 and TiH<sub>2</sub>. They were in agreement to better than 0.5 percent.

### **A.5.2 Compression modulus**

Compression testing was performed on a total of 11 porous test samples. These samples consisted of a series of cylinders roughly 1.0 cm in diameter 1.2 cm in height. These test samples were machined using standard EDM procedures from four larger cylindrical products of foaming runs. These cylinders were 1.8 cm in diameter and 2.5 cm in length. Five test samples with a chemical composition containing one percent TiH<sub>2</sub> came from two foaming runs while the six samples that came from the other two foaming runs had a two percent TiH<sub>2</sub> content.

Data from these compression tests were plotted in a format to determine if it conformed to the standard relationship for open-cell foams given below where "E" and "ρ" stand for modulus and density values respectively. In this expression, the values preceded by an asterisk indicate the experimental values for the foam samples while the values with the "s" subscript indicate values of the non-porous material.

$$\left(\frac{E^*}{E_s}\right) \approx \left(\frac{\rho^*}{\rho_s}\right)^2 \quad (\text{A.5.2.1})$$

If the logarithm of each side of the above expression is taken, it reduces to

$$\text{Log}(E^*) = 2\text{Log}(\rho^*) + k \quad (\text{A.5.2.2})$$

A log-log plot of modulus versus sample density is shown in Figure A.5.2-1. Although there is considerable scatter in the data, a best-fit straight line results in a slope close to 2.0. Given the statistical variation in pore size, non-random pore orientation and presence of defects, the degree of scatter is not unexpected.

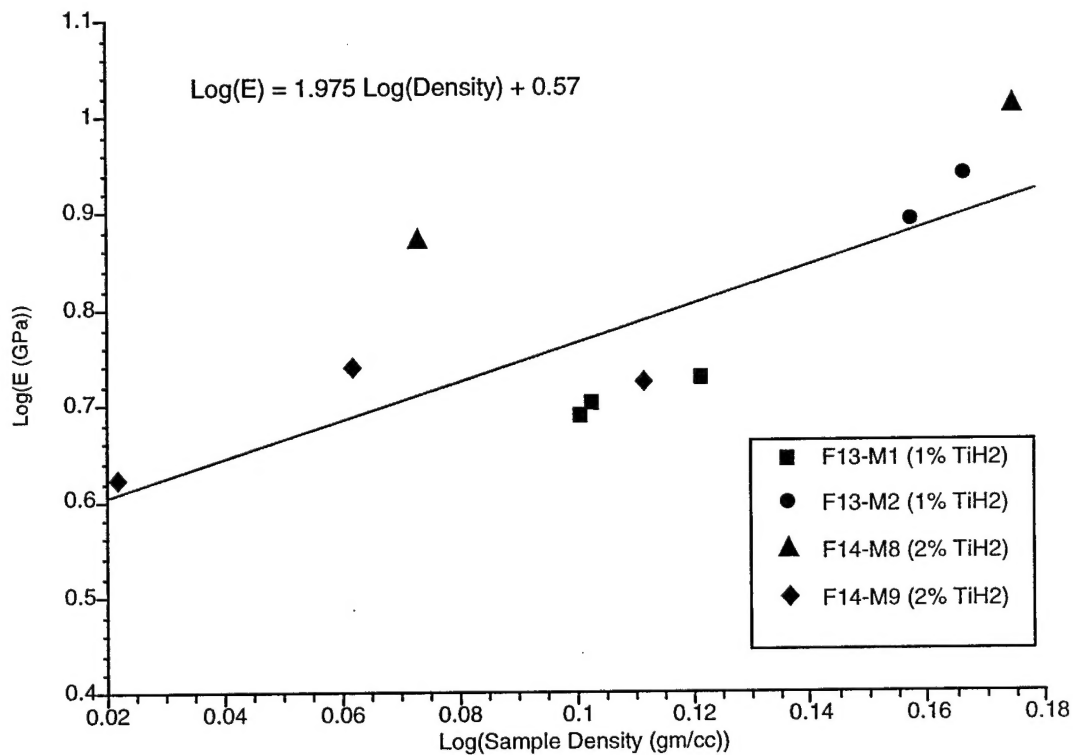


Figure A.5.2-1 Log-log plot of modulus Vs sample density for  $\text{TiH}_2$ -2124 Aluminum test samples.

## **APPENDIX B**

### **HIGH TEMPERATURE SPM CONCEPT EVALUATION**

The purpose of this task was to characterize the structure of a high temperature porous metal and determine preliminary room temperature mechanical properties.

McDonnell-Douglas had agreed, during the proposal process, to supply samples of their titanium SPM material for evaluation by UTRC under this program. McDonnell is manufacturing this material under their ONR Contract supporting DARPA's Advanced Materials Partnership (AMP) Program entitled 'Ultra-Lightweight Metals Materials,' and was to be made available for characterization in May 1996. At the time of the program redirection, no material had been supplied by Mc Donnell.



## APPENDIX C

The following results summarize the computed F statistic for comparisons made between categories in intersecting rows and columns. The ANOVA routine that is employed limits the measurement comparison to only one category, that is either between locations within a given product or between two products in the same location. Shaded areas indicate categories which could not be analyzed. Asterisks indicate the key results.

**Table C.1 Computed F-statistic Values for Wall Thickness Measurements in the L Direction**

	HDPe	HDPm	LDPe	Cm	Ct
HDPm	5.87*				
LDPe	0.10				
LDPm		4.42	0.026		
Cb				2.28	2.53
Cm					0.07

\* = significant at 0.05 level

**Table C.2 Computed F-statistic Values for Wall Thickness Measurements in the T Direction**

	HDPe	HDPm	LDPe	Cm	Ct
HDPm	4.38				
LDPe	0.75				
LDPm		1.87	0.13		
Cb				1.31	0.03
Cm					573*

\* = significant at 0.05 level

**Table C.3 Computed F-statistic Values for Cell Area Measurements in the L direction**

	HDPe	HDPm	LDPe	Cm	Ct
HDPm	0.38				
LDPe	9.29*				
LDPm		63.84*	0.65		
Cb				6.66	37*
Cm					0.67

\* = significant at 0.05 level

**Table C.4 Computed F-statistic Values for Cell Area Measurements in the T direction**

	HDPe	HDPm	LDPe	Cm	Ct
HDPm	3.84				
LDPe	2.74				
LDPm		16.68*	1.99		
Cb				0.32	2.54
Cm					0.54

\* = significant at 0.05 level